Iowa State University
Digital Repository

2013

Templated synthesis of nickel nanoparticles: Toward heterostructured nanocomposites for efficient hydrogen storage

Nicholas Nelson
Iowa State University

Follow this and additional works at: https://lib.dr.iastate.edu/etd

Part of the Nanoscience and Nanotechnology Commons, and the Oil, Gas, and Energy Commons

Templated synthesis of nickel nanoparticles: Toward heterostructured nanocomposites for efficient hydrogen storage

by

Nicholas Cole Nelson

A thesis submitted to the graduate faculty

in partial fulfillment of the requirements for the degree of

MASTER OF SCIENCE

Major: Chemistry

Program of Study Committee:
Javier Vela, Major Professor
Gordon Miller
Klaus Schmidt-Rohr

Iowa State University
Ames, Iowa
2013

TABLE OF CONTENTS

ACKNOWLEDGEMENTS

ABSTRACT

The world is currently facing an energy and environmental crisis for which new technologies are needed. Development of cost-competitive materials for catalysis and hydrogen storage on-board motor vehicles is crucial to lead subsequent generations into a more sustainable and energy independent future. This thesis presents work toward the scalable synthesis of bimetallic heterostructures that can enable hydrogen to compete with carbonaceous fuels by meeting the necessary gravimetric and volumetric energy densities and by enhancing hydrogen sorption/desorption kinetics near ambient temperatures and pressures. Utilizing the well-known phenomenon of hydrogen spillover, these bimetallic heterostructures could work by lowering the activation energy for hydrogenation and dehydrogenation of metals. Herein, we report a novel method for the scalable synthesis of silica templated zero-valent nickel particles (Ni$\subset$SiO$_2$) that hold promise for the synthesis of nickel nanorods for use in bimetallic heterostructures for hydrogen storage. Our synthesis proceeds by chemical reduction of a nickel-hydrazine complex with sodium borohydride followed by calcination under hydrogen gas to yield silica encapsulated nickel particles. Transmission electron microscopy and powder X-ray diffraction were used to characterize the general morphology of the resultant nanocapsules as well as the crystalline phases of the incorporated Ni^0 nanocrystals. The structures display strong magnetic behavior at room temperature and preliminary data suggests nickel particle size can be controlled by varying the amount of nickel precursor used in the synthesis. Calcination under different environments and TEM analysis

provides evidence for an atomic migration mechanism of particle formation.

Ni⊂SiO$_2$ nanocapsules were used as seeds to induce heterogeneous nucleation and subsequent growth within the nanocapsule *via* electroless nickel plating. Nickel nanoparticle growth occurs under high temperature alkaline conditions, however silica nanocapsule integrity is not maintained due to the incompatibility of silica with the growth conditions. Silica nanocapsule integrity is maintained under low temperature neutral conditions, but nickel particle growth is not observed. Through FTIR and UV/Vis analysis, we show the degree of crosslinking and condensation increases in calcined silica compared to as-synthesized silica. We propose the increased density of the silica nanocapsule hinders mass transfer of the bulky nickel precursor complex from solution and onto the surface of the "catalytic" zero-valent nickel seed within the nanocapsule cavity. Decreasing the density of the silica nanocapsule can be achieved through co-condensation of tetraethylorthosilicate with an alkyl functionalized silane followed by calcination to remove the organic component or by chemical etching in alkaline solution, but will not be addressed in this thesis.

CHAPTER 1. INTRODUCTION

Motivation: The Hydrogen Economy

Air quality has become a hot topic in the last few decades because of its effect on public health, ecosystem stability, and global climate change. One of the major contributors to air quality, or lack thereof, is motor vehicle emissions. It is estimated that 14% of worldwide greenhouse gas emissions and 19% of CO_2 emissions can be attributed to motor vehicles and the percentage is expected to increase with the quick economic growth of developing countries. [1] Hydrogen (H_2) has been proposed as an alternative fuel, especially for use in the transportation sector, because its combustion produces water and the most energy released by any fuel on a mass basis (Scheme 1).[2]

Scheme 1.

$$H_2 + \tfrac{1}{2} O_2 \longrightarrow H_2O + heat, \ \Delta H = -285.8 \ kJ \ mol^{-1} \ at \ 25°C$$

$$\Delta G = -237.2 \ kJ \ mol^{-1} \ at \ 25°C$$
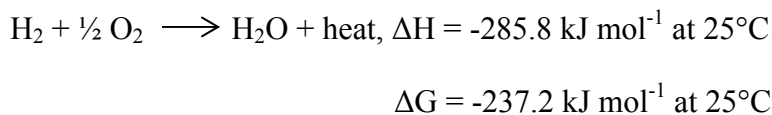
There are numerous advantages to use hydrogen as a fuel for vehicles including, but not limited to: Hydrogen's combustion by-products are restricted to water vapor and minute quantities of nitrogen oxides when used in an internal combustion engine (ICE) and only water vapor when used in a fuel cell (FC); hydrogen can be obtained from a wide assortment of primary energy sources making it readily accessible in most parts of the world; and, hydrogen is the most abundant element in the universe. With all of these advantages in hand, hydrogen technology has surged to the forefront of energy research and development.

Although hydrogen is a good alternative energy candidate, there are major technological hurdles that need to be overcome in order to realize its full potential. The overwhelming majority of hydrogen is chemically bound in the form of water and hydrocarbons, and therefore energy (and money) must be spent to isolate H_2 from other sources. Cheap and efficient H_2 production methods from renewable energy sources, either directly or indirectly, are needed to make H_2 more competitive with carbonaceous fuels and eventually wean us from our dependence on them. Another problem becomes how to efficiently, effectively, and safely store hydrogen on-board a vehicle. In order to implement hydrogen as a transportation fuel, a suitable storage device must meet several requirements outlined by the United States (US) Department of Energy (DOE) (Table 1).[3] High gravimetric energy density and high volumetric energy density are both required to provide long vehicle range comparable to gasoline and allow for adequate passenger room. A working system must also exhibit refueling times comparable to gasoline and function at or near ambient temperature and pressure to ensure passenger safety as well as maintain energy efficiency. In addition, whatever material the storage device is made from, it must not be prone to poisoning by oxygen. The development of low cost hydrogen production methods and storage materials with high gravimetric and volumetric energy density, quick fill times, and ambient operating conditions is thus critical to realizing zero-emission vehicles.

There are several candidates for materials or methods possessing attributes that meet the DOE hydrogen storage goals. Of these, solid-state devices (*e.g.* metallic hydrides) are seemingly the best candidates due to their outstanding high volumetric energy densities, adequate gravimetric energy densities, indefinite storage capability, and

safety. Unfortunately, metallic hydrides lie in a thermodynamic well (*i.e.,* they are very stable) and oftentimes the dehydrogenation temperature and pressure conditions used are undesirable for on-board storage. It has been demonstrated that certain transition metal dopants can vastly improve the sorption and desorption kinetics of metal hydride containing compounds.[4,5,6,7,8] Fabrication of other novel solid-state materials and devices with good sorption-desorption kinetics remains an outstanding goal and challenge.

Table 1. DOE Targets for On-board Hydrogen Storage
Systems for Light-Duty Vehicles

Storage Parameter	Ultimate Goal
System gravimetric capacity	0.075 kg H_2 kg^{-1} system 2.5 kWh kg^{-1}
System volumetric capacity	0.070 kg H_2 L^{-1} system 2.3 kWh L^{-1}
System fill time(5kg)	2.5 min
Durability/operability	
• Operating temperature	-40/60 °C
• Min/max delivery temperature	-40/85 °C
• Operational cycle life	1500 cycles
• Min delivery pressure from storage system	3FC/35ICE bar (abs)
• Max delivery pressure from storage system	12FC/100ICE bar (abs)

The world is currently facing an energy and environmental crisis for which new technologies are needed. Long-term development and sustainability will become much easier if we are able to find alternative energy sources and utilize them efficiently. Advancing the field of hydrogen storage with new materials could allow for more

sustainable energy and environmental practices, achieve energy independence, and assure economic prosperity for future generations.

## Hydrogen Storage Methods

Overview

An immediate reason for the nonexistence of a hydrogen fuel network is the lack of an efficient and effective on-board-vehicle hydrogen storage system. At ambient temperature and pressure, 1 kg of hydrogen gas (about a gasoline gallon equivalent) occupies a volume of over 3,000 gal[9]. Clearly, the low density of hydrogen gas restricts its practical and widespread use as a transportation fuel today and innovative storage technologies are needed to allow for efficient and operative storage. Hydrogen can be stored as a gas, a cryogenic liquid, physisorbed on large specific surface area structures, and bound to other elements (*e.g.* metallic hydrides).

Liquefaction and Compression

Liquefied hydrogen offers the advantage of possessing a relatively high density at ambient pressure (71.0 kg/m^3), but liquefaction is an energy intensive process. The simplified phase diagram in Figure 1 shows the boiling point of liquid hydrogen is 20.4 K at 1 bar and the critical point is 33.2 K.[10] Liquefaction of hydrogen gas from room temperature costs about 15 kW-h$_e$/kg, which is about 30% of the lower heating value (LHV) for hydrogen combustion.[2] In addition, the tanks must be well insulated adding to the overall system weight.[2] Furthermore, liquid hydrogen cannot be contained in a closed system due to boil off. At room temperature over 75% of hydrogen exists as ortho-

hydrogen that becomes unstable when cooled to liquid temperatures.[11] Ortho-hydrogen undergoes a transition to para-hydrogen with the release of heat which is greater than the latent heat of vaporization for hydrogen and thereby contributes to vaporization of liquid hydrogen.

Compression is a convenient and familiar way to store hydrogen, but the cost is far too high to become practical. High pressure tanks built of carbon fiber can withstand pressures up to 700 atmosphere (11 wt. %) and compression only costs 10% of the LHV for hydrogen combustion; however, the tank fabrication cost is $3000/kg H_2.[2] Unless there are significant advances in reducing the cost of liquefaction or the materials used to construct high pressure cylinders, there will need to be an alternative to these familiar methods of hydrogen storage for use in the transportation industry.
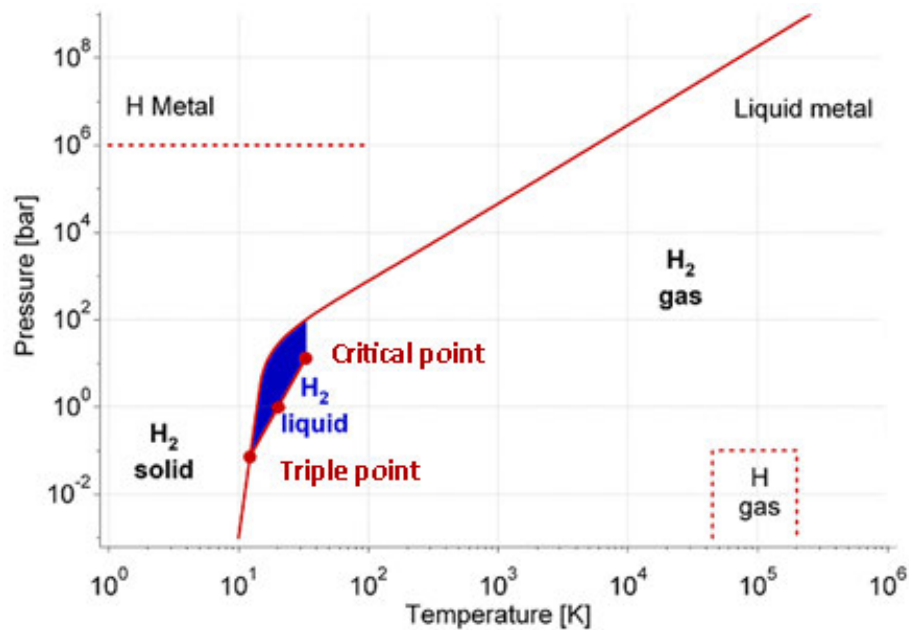
Figure 1 Hydrogen phase diagram.[10]

Physisorption

Physical adsorption is the process by which gas molecules bind with an adsorbent *via* van der Waals (vdW) forces. This process is reversible due to the weak interaction between the absorbed species and the adsorbent (*i.e.* there are no chemical bonds being formed). Adsorption of supercritical gases on solid surfaces takes place through monolayer adsorption according to Brunauer-Emmett-Teller (BET) theory.[12] The first layer of gas molecules absorbed on the surface has a unique absorption energy characteristic of a gas-solid interaction. Subsequent layers have an absorption energy that differs from the first layer due to adsorbate-adsorbate interactions. As the number of layers increases the absorption energy approaches the latent heat of condensation for the gas.[13] However, supercritical gases like hydrogen cannot undergo condensation processes above their critical temperature.[14]

Hydrogen storage materials that work through physisorption alleviate thermal management problems associated with other storage methods because hydrogen is so weakly bound, resulting in reaction enthalpies for the hydrogenated and dehydrogenated forms to be small. However, the temperature must be reduced near liquid nitrogen temperature in order to achieve sufficient hydrogen absorption. Above these temperatures there is not enough hydrogen-adsorbate interaction to obtain any useful level of adsorption. The binding energy needed for physisorption of hydrogen at room temperature is 0.15-0.30 eV and typical vdW binding energies for hydrogen at room temperature are usually a few times smaller than the lower limit.[9] Engineering of materials that satisfy the binding energy requirements at room temperature remains a significant challenge. In addition, the specific surface area of the material must become

very large (>2600 m^2/g) and the walls between any nanometer-sized pores must approach atomic thickness in order to increase gravimetric energy density.[15] Current research in this area is focused on metal-organic frameworks (MOFs) which to date have exhibited surface areas of 7000 m^2/g. [16] However, MOFs are still unable to achieve the necessary binding energies and therefore must still be cooled to liquid nitrogen temperatures.

Metallic Hydrides

There are two types of metallic hydrides proposed for hydrogen storage materials: Metal hydrides and complex hydrides. The main difference is the type of bonding that occurs. Most metal hydrides are crystalline and exhibit ionic bonding between cationic metal and anionic interstitial hydrogen (*e.g.* LiH, MgH$_2$, AlH$_3$,). Complex hydrides typically consist of more than one metal or are a combination of a metal and a metalloid. They are characterized by ionic bonding between a metal cation and a molecular anion containing the hydride. The bonding in the anionic component is preferentially covalent (*e.g.* NaAlH$_4$, LiBH$_4$, Mg$_2$FeH$_6$). The advantages of metallic hydrides include their excellent volumetric energy densities and relative safety compared to liquefaction and compression. In addition, some complex hydrides can reversibly absorb hydrogen at or near ambient pressure and temperature, but in all cases the complex contains a transition metal which has devastating effects on gravimetric energy density. For example, LaNi$_5$H$_6$ has a volumetric energy density of 115 kg/L and can reversibly store hydrogen at ambient pressure and temperature.[9] Unfortunately, the gravimetric energy density is only 1.4%. Therefore, special attention is has been paid to hydrides of light metals (*e.g.* B, Na, Mg, Al).

Light metallic hydrides were long thought to be relatively inert toward hydrogen loss near ambient temperature and pressure. Pioneering work by Bogdanovic *et al.* showed that doping sodium alanates with titanium resulted in faster sorption-desorption kinetics at a given temperature and pressure (Figure 2).[4,17] However, the gravimetric energy density of this system was not high enough to reach the goals initially set by the DOE for use in transportation.
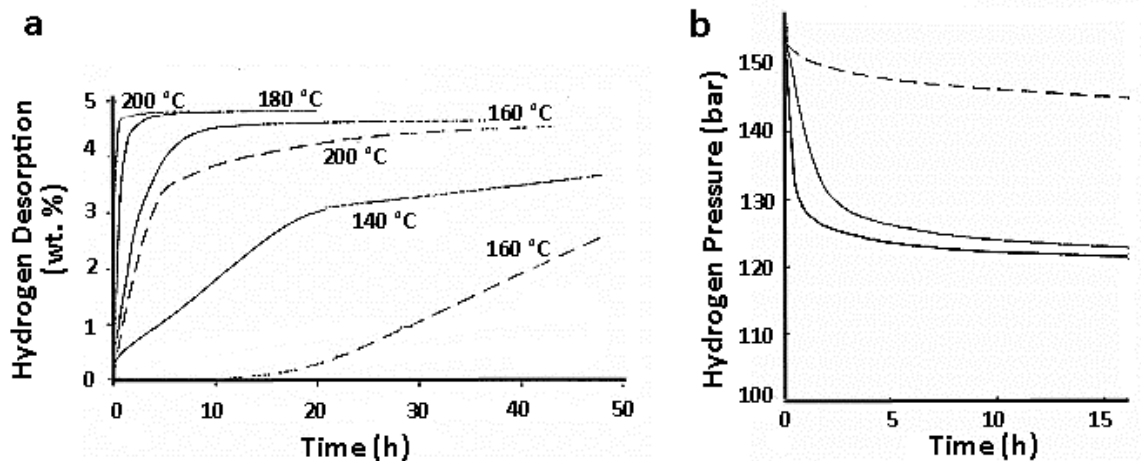
Figure 2. (a) Hydrogen desorption versus time at different temperatures for Ti doped NaAlH$_4$ (——) and undoped NaAlH$_4$ (------); (b) Hydrogen adsorption (170°C/152 bar) as a function of time for Ti doped NaAlH$_4$ (——) and undoped NaAlH$_4$ (------).[4]

One main focus of hydrogen storage technology is to develop metallic hydrides meeting gravimetric energy density constraints that also show good kinetics for reversible hydrogen sorption-desorption at or near ambient pressure and temperature. Figure 3 lists the most promising metallic hydrides for use as hydrogen storage materials, as well as how these compare to some of the other storage methods available.[9] Clearly there are several metallic and complex hydrides that meet the gravimetric and volumetric energy

constraints, but to date none have met the necessary kinetic and thermodynamic constraints. Doping light metallic hydrides with dehydrogenation/hydrogenation metal catalysts is one of the most practical ways to meet the kinetic, thermodynamic, gravimetric, and volumetric energy requirements for hydrogen storage materials.

Bimetallic Nanocomposites for Efficient Hydrogen Storage

Hydrogen Spillover

An phenomenon of interest for hydrogen storage known as spillover was first reported by several groups independently in the 1960s.[18,19,20,21,22,23] Sinfelt and Lucchesi[24] found the rate of hydrogenation of ethylene was greatly enhanced when a Pt/SiO$_2$ catalyst was mixed with Al$_2$O$_3$ compared to the catalyst mixed with SiO$_2$. The synergistic effect between Pt/SiO$_2$ and Al$_2$O$_3$ could not be explained by the additive catalytic effects of all three species. Since both SiO$_2$ and Al$_2$O$_3$ are inert toward hydrogenation of ethylene, but only Al$_2$O$_3$ chemisorbs ethylene under the conditions used, the authors concluded that the enhanced rate of ethane formation must be due to the dissociation of hydrogen on Pt and subsequent migration to the Al$_2$O$_3$ substrate and reduction of chemisorbed ethylene. Subsequent studies led to the following definition: "Spillover involves the transport of an active species which is adsorbed or formed on a first phase onto another phase that does not adsorb or form the species under the same conditions."[25]
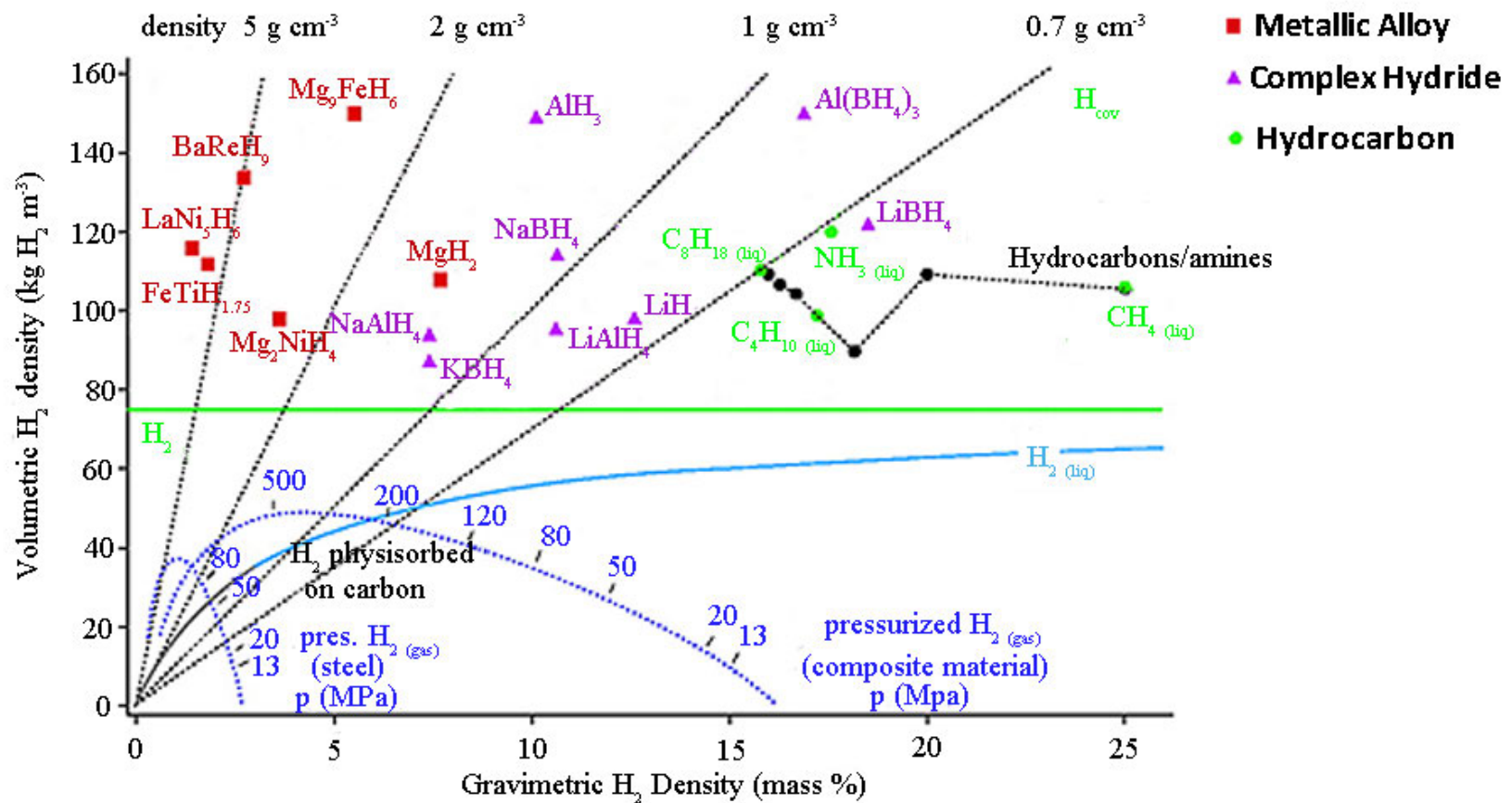
.

Figure 3. Volumetric and gravimetric hydrogen density of hydrogen storage materials.[9]

Hydrogen spillover can occur between a metal and a metal oxide[18] or between two metals[26] and is believed to occur through three principal steps (Scheme 2): (1) Dissociative chemisorption of hydrogen gas on a metal surface, (2) migration of hydrogen atoms to the metal-substrate interface, (3) and diffusion of hydrogen atoms across the metal-substrate interface.[27] Often times, the rate-limiting step and key species in hydrogen spillover are surface diffusion of hydrogen atoms across the metal-substrate interface, or more generally the activator-acceptor interface (Figure 4).[22,28] The mobility of hydrogen atoms on the acceptor surface gives rise to catalytic behavior and also "cleans" the surface of the metal catalyst, allowing another hydrogen molecule to undergo dissociative chemisorption. The process of spillover is reversible, whereby the hydrogen atoms diffuse from the substrate to the metal and then undergo recombination and desorption.

Scheme 2.
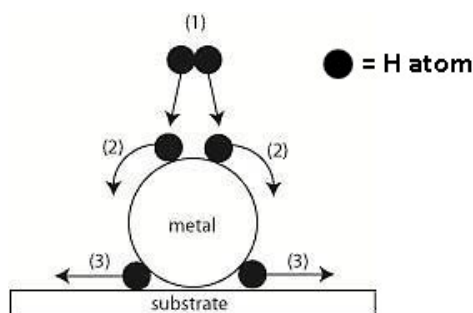
When the hydrogen concentration in certain metals exceeds the saturation concentration a hydride phase is formed. Studies have shown hydride nuclei normally "precipitate" near the metal surface, and the rate of near-surface hydride nuclei formation depend on the rate of hydrogen dissociation at the gas-metal interface.[29] When the growing hydride nuclei overlap to form continuous hydride layers, the kinetics no longer

depend upon the nucleation parameters, but switch to a so-called 'shrinking core' function.[29] The main intrinsic kinetic parameter becomes the diffusion of hydrogen atom to the metal-metal hydride interface. Certain metals (*e.g.* Group 10) are able to dissociate hydrogen faster than other metals and this property can be exploited to possibly increase the hydrogenation rate of other metals *via* hydrogen spillover. For example, doping Mg^0 with Ni^0 could increase the rate of MgH_2 formation because Ni^0 can catalyze the dissociation of hydrogen to form the initial near-surface hydride nuclei. The hydrogen atoms could then diffuse to the metal-metal hydride interface through hydrogen spillover. Minimizing the distance between the nickel active sites could be used to decrease the time necessary for the hydrogen atoms to reach the metal-metal hydride interface, thus facilitating and speeding the kinetics of hydrogenation. Dehydrogenation kinetics (the reverse process) could also benefit from a similar series of steps. Hydrogen spillover is therefore a key mechanism for building materials that exhibit reversible, fast hydrogenation/dehydrogenation kinetics.
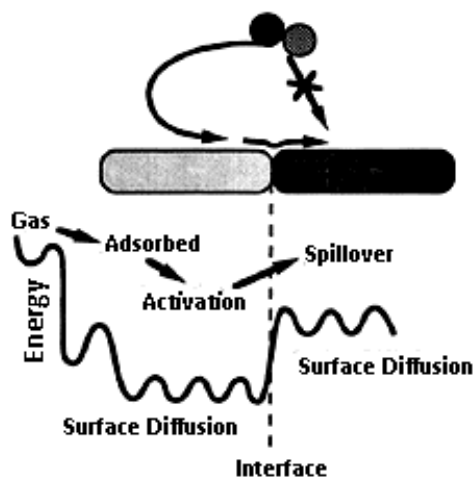
Figure 4. Qualitative energy diagram for hydrogen spillover process.[18]

Bimetallic Structures

Utilizing hydrogen spillover to enhance sorption-desorption kinetics of hydride forming metals is a plausible approach to develop better hydrogen storage materials. Studies focused on doping light metals (Mg, Al) with transition metals (Ti, V, Ni, Mn, Fe) showed a marked increase in sorption-desorption kinetics of molecular hydrogen and lower dehydriding temperatures.[5,6,7,8] Tan *et al.*[30,31,32] showed that doping magnesium with iron (Mg-Fe) in the form of thin films capped with palladium resulted in significantly enhanced hydrogen sorption-desorption kinetics and lower activation energy compared to the undoped Mg films capped with palladium. In this system, palladium serves two purposes: It acts as a protecting layer to prevent surface passivation of the Mg/MgH_2 film and as a catalyst for hydrogen dissociation and the resultant spillover.[33] The embedded iron is thought to act as a secondary metal catalyst to facilitate the diffusion of hydrogen atoms through the MgH_2 phase. Furthermore, time resolved infrared (IR) measurements on wedge-shaped Mg-Fe thin films showed the rate of MgH_2 formation increases with increasing temperature and decreasing film thickness. The rate limiting step for phase front migration is diffusion of hydrogen atoms through the MgH_2 layer to the Mg/MgH_2 boundary. The increase in rate of formation of MgH_2 as the film thickness decreases is due to a larger fraction of the atoms occupying surface sites, which minimizes the extent to which hydrogen atoms must migrate through the hydride phase. Volumetric pressure-composition isotherms (PCI) on 600 nm thick Mg-Fe thin films showed the enthalpy of adsorption-desorption (66.9 kJ mol^{-1}) was less than bulk Mg (76 kJ mol^{-1}) or thin films of undoped Mg (80kJ mol^{-1}). In addition, the Mg-Fe films exhibited good absorption-desorption hysteresis through two cycling experiments which

is another necessary property of hydrogen storage materials. Bimetallic structures have thus shown enhanced kinetic hydrogenation rates and decreased thermodynamic hydrogenation barriers allowing hydrogenation to occur in less than one minute and 150°C.

Another possible benefit of bimetallic structures is the development of a destabilized phase that could lower the heat of hydride formation. Dehydrogenation of metal hydrides is an energy intensive process and to decrease the enthalpy of formation the hydride complex needs to be activated or 'destabilized'. The metal catalyst responsible for hydrogen spillover could also form a new compound with the parent metal and hydrogen resulting in a destabilized product exhibiting decreased heats of formation for the metal and metal hydride. For example, a reduction of hydrogen desorption temperature was observed for nanocomposites of 85 wt. % Mg-15 wt. % $Mg_2Ni_{1-x}Fe_x$ (x=0, 0.1, and 0.3).[34] The enhanced desorption kinetics of the composite were attributed to a new hydride phase forming from the ternary intermetallic dopant.

Managing the heat evolved during the hydriding reaction is another crucial step toward meeting hydrogen storage goals. Bimetallic structures offer the advantage of good thermal conductivity which can help improve efficiency and sorption-desorption kinetics. The DOE has noted that the hydrogenation rate should be 1.98 kmol H_2 min^{-1} (Table 1). For Mg, with an enthalpy for MgH_2 formation of 75 kJ mol^{-1} H_2, over 300 MJ of heat is evolved assuming a fill time of 2.5 minutes. Supposing no heat removal, the temperature rise can be estimated from $\Delta T = Q/(nc)$, where n is the number of moles, c is the specific heat and Q is the total heat supplied to the system. Metallic Mg has a specific heat of 24.9 J mol^{-1} K^{-1} and thus gives temperatures on the order of 1000°C. [35,36] At these

temperatures hydride formation will cease to occur and sintering will become a problem. However, metal hydrogenation/dehydrogenation catalyst dopants such as Fe or Ni have moderate thermal conductivities and the metal matrix could help dissipate the heat evolved during the hydriding reaction leading to more facile kinetics.

Benefits of Nanoarchitectures

Nanoscale materials are currently being researched as a replacement for bulk hydrogen storage materials due to their unique chemical, physical, thermodynamic, and kinetic properties.[37] These materials help to address numerous problems associated with bulk metal hydrides: Inadequate storage capacity, sluggish sorption-desorption kinetics, and high dehydriding temperatures. Typically, metal hydride complexes are fairly stable and do not usually undergo dehydrogenation until temperatures above 200°C. [8] This is detrimental to the overall efficiency of the storage material. However, nanoparticle versions of these materials have considerably larger surface areas compared to the bulk and as such they have a higher surface energy. This helps to lower the heat of formation both for the metal and the metal hydride. When the surface energy of the hydride is greater than that of the metal, a portion of the heat of formation will be stored as excess surface energy permitting the heat released upon hydride formation to decrease and the heat needed for dehydrogenation to be diminished which improves efficiency compared to bulk materials.[8] Furthermore, nanomaterials offer greater surface area and/or porosity compared to their bulk counterparts, which translates into more hydrogen adsorption sites (*i.e.* increased kinetics). Smaller particles also enhance sorption-desorption kinetics because the hydrogen atom has less material to diffuse through to fully accomplish the

conversion to the metal hydride and likewise when going from the metal hydride to the metal. Together, these observations support the idea that bimetallic nanomaterials could revolutionize the field of reversible hydrogen storage and enable the use of hydrogen as a clean energy source.

Goals and Approach

As outlined above, development of materials that store hydrogen effectively and allow for fast, reversible hydrogen sorption-desorption under ambient conditions is needed in order to be able to use hydrogen as a way to reach a more sustainable and energy independent future. To achieve the necessary hydrogen storage goals set forth by the DOE, we propose a bimetallic heterostructured nanocomposite with interpenetrating transition metal veins (Figure 5). The interpenetrating veins will be made of known hydrogenation/dehydrogenation catalysts and serve as dissociation sites for molecular hydrogen. This could help reduce the kinetic barrier of hydride formation for the parent metal (*e.g.* Mg) (Figure 5) by catalyzing the formation of initial near-surface hydride nuclei through hydrogen spillover. The geometry of the interpenetrating network of veins could also help reduce the time that it takes for hydrogen atoms to diffuse to the metal-metal hydride interface by reducing the effective bulk of the parent metal. There are three main objectives that need to be realized for successful synthesis of the proposed novel bimetallic heterostructures:

1. Research and development of a scalable, size-tunable synthesis of
    hydrogenation/dehydrogenation metal nanorod catalysts to facilitate quick
    conversion of metal to metal-hydride and vice versa.

2. Research and development of a method to successfully encapsulate metal
    nanocatalysts within particles or aggregates made of lighter hydride-forming
    metals (Li, B, Na, Mg, Al), or combinations thereof.

3. Investigation of hydrogenation/dehydrogenation catalytic and uptake
    experiments needed in order to optimize the numerous combinations and
    conditions that could be exploited.

Success of this research will be an enormous technological leap from the current status of
on-board hydrogen storage materials, enabling the use of a clean and renewable fuel (H_2)
for transportation purposes.
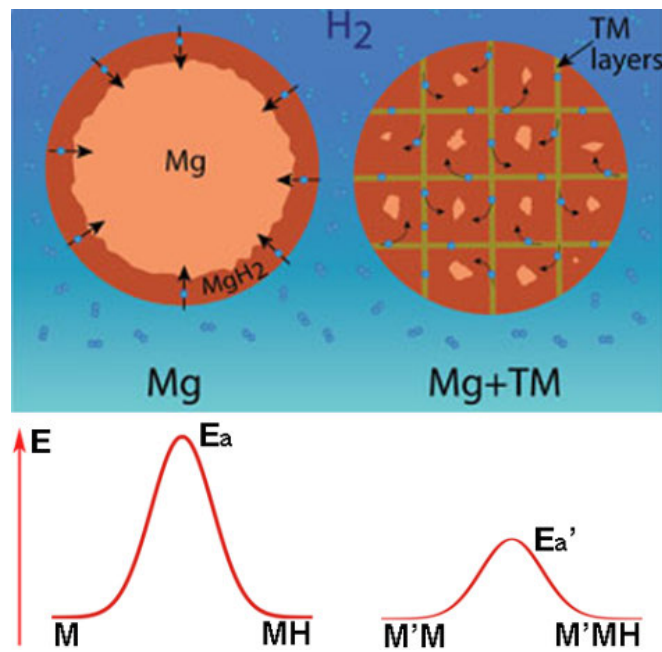
Figure 5. Schematic of bimetallic heterostructured nanocomposite for hydrogen storage.

The first step in the synthesis of bimetallic heterostructured hydrogen storage materials is to investigate and develop a robust, scalable synthesis of size-controllable metal nanorods (Fe, Co, Ni, Rh, Pd, Pt, Ir, Ti, V). Ideally, this new method will produce the desired nanorods simply by varying the metal precursor and reductant used in their synthesis. A hard template approach is an ideal way to achieve the desired attributes of the aforementioned synthesis. The already known and available syntheses of size tunable templates allows for the possibility to fill such templates with any metal of interest, thus producing an inner cavity replica (duplicate) of the template in a single step. Silica is widely used as a hard template due to its hydrophilicity, thermal stability, chemical robustness, and ease of synthesis and processability. A silica shell structure also offers the advantage of processability in a wide range of solvents depending on the surface functionalities of the shell and can also protect against metal sintering or coalescence. Size-controlled, industrially scalable synthesis of silica nanocapsules has recently been demonstrated[38] and is used as a hard template to confine the growth of zero-valent metals in the present work.

The synthesis of zero-valent metal nanorods is attempted through colloidal chemical methods. The silica nanocapsules are fabricated by condensation and hydrolysis of silica precursor onto a 1D nickel complex. Because nickel is already present inside the nanocapsule and is a fairly reactive metal, we employ chemical reduction of this same nickel complex. For other metals (Fe, Co, Ti, V, etc.) a seeded growth process could be employed, but is not explored here. A general approach for the seeded growth process requires functionalizing the inner surface of the silica nanocapsules with groups that have a strong affinity for the metal of interest (*i.e.* Fe, Co, Ti, and V). Treatment of internally

functionalized silica nanocapsules with a solution of metal precursor could allow for retention of specific metal species inside the nanocapsule. Reduction of the thus retained metals would yield zero-valent metal clusters that can act as seeds for heterogeneous nucleation and subsequent growth. Retrieval of zero-valent nanorods can be achieved by chemical etching.

After optimizing the synthesis of the nanorods, the next step would be encapsulation of the nanorods in a light metal that has a high affinity for hydride formation. There is much precedent for metal-metal epitaxial growth in the literature,[39,40] but to date this step in the process has not been explored. Once established, we could begin to experiment with different types of metals and loadings to find optimal conditions for hydrogen storage. This research could lead to the development of hydrogen storage materials that will at the minimum become a model system for future hydrogen storage solid-state materials. Ideally, these materials will result in unprecedented hydrogen sorption/desorption kinetics near ambient conditions while satisfying the gravimetric energy density needs to become a viable solution for obtaining energy independence and economic prosperity.

CHAPTER 2. HARD TEMPLATE APPROACH FOR THE SYNTHESIS OF METAL NANORODS

Introduction

There are several literature examples citing the synthesis of one-dimensional (1D) nanomaterials.[41] Six methods commonly employed include: (1) Intrinsic anisotropic crystallization of the material, (2) vapor-liquid-solid (VLS) processes from liquid droplet seeds, (3) using a 1D template to direct the formation of 1D structures, (4) using ligands to stabilize certain growing facets leading to anisotropic growth, (5) self-assembly of zero-dimensional nanostructures, and (6) size reduction of 1D microstructures. Template-directed synthesis represents a simple, high-throughput, potentially cost-effective and straightforward approach to 1D nanostructure growth without complicated, ill-defined chemical methods and conditions that often accompany other methods. In this approach, the template serves as a rigid structure in which the desired material is generated within or around. The morphology of the new material generated is therefore complementary to the original template. The method is generic and template removal is often achieved through chemical etching (hard templating) or calcination (soft templating).

Templates commonly used include the step edges or V-grooves present on the surfaces of solid substrates,[42,43] the channels and pores of mesoporous materials,[44] solution-born micelles,[45] biological macromolecules such as DNA strains,[46, 47] and pre-existing nanostructures synthesized using one of the aforementioned methods.[48] Templating against the features of a solid substrate is regularly exploited for the synthesis of nanowires when aspect ratio control is not important or critical. In solution-phase,

certain surfactants are known to self-assemble into cylindrical or rod shaped micelles when their concentration exceeds a certain value and their anisotropic morphology can be used as a template. However, the preparation and removal of the micellar phase is frequently difficult and tedious. Biological templates offer a unique way to achieve 1D growth, and their use is conceptually similar to templating against pre-existing nanostructures described below. Templating against the channels of mesoporous materials usually results in polycrystalline materials. In addition, the method offers the major advantage of aspect ratio control, low size dispersion, and provides potential large-scale production.

The most common mesoporous templates include track-etched polymer films, carbon nanotubes (CNTs), alumina films, and mesoporous silica. Track-etched polymer films require bombarding polymer films with heavy ions (from nuclear fission) to create damaged spots on the surface of the film and subsequent chemical etching to generate uniform, cylindrical pores piercing the membrane film.[41] The films are easily removed through pyrolysis at elevated temperatures, but the resultant nanorods can be distorted or broken due to template removal before the complete densification of the rods.[49] CNTs have also been used as templates in the synthesis of 1D metals.[50,51] However, well-controlled aspect ratios have not been achieved with this approach and template removal remains a challenge. Another commonly used template is anodized aluminum oxide (AAO). Anodization of aluminum in a strong acid electrolyte results in a self-organized process and formation of uniform pores. Pore dimensions are controlled by the anodization technique and the electro-chemical parameters employed. The diameters and lengths of the pores can be as small as 5 nm and 100 nm, respectively; however,

improvements must be made to increase the area of the ordered domains. Moreover, the fabrication time for long-range ordered domains must be decreased to increase cost-efficiency and become industrially scalable.[52] One other commonly employed method for the synthesis of 1D materials consists of templating against the interior channels or pores of mesoporous silica nanoparticles (MSNs). Silica offers the advantage of high thermal stability, hydrophilicity, susceptibility to selective surface functionalization of inner and outer surfaces, wall structure porosity, facile synthesis, optical transparency (making it useful as a template in photochemical syntheses), and most importantly, scalability. By choosing the correct type of mesoporous silica material, the aspect ratio of 1D materials templated within their structure can be precisely controlled with reasonable monodispersity. Together, these attributes are ideal for synthesizing metal nanorods for bimetallic heterostructured hydrogen storage materials.

Templating against the channels in MSNs (*e.g.* MCM or SBA) to yield zero-valent metals (Fe, Co, Ni, Cu, Pd, Pt, Au, Ag) has been demonstrated in the literature.[44,53,54,55,56] Typical procedures for the synthesis and harvesting of 1D metals involve three basic steps: Impregnation with a metal precursor, reduction of the metal precursor inside the channels, and subsequent etching of the template to yield nanostructures with high aspect ratio (1D) morphologies. For example, Chao *et al.*,[44] functionalized the surfaces of MCM-41 with organic ammonium chloride salts followed by the introduction of MCl_m^{n-} salts, resulting in the exchange with chloride anions and subsequent adsorption of metal chlorides onto the pore surface. Reduction of the metal salts by calcination in an H_2 atmosphere yielded metal nuclei inside mesoporous silica. Further growth of the primary metal nuclei resulted in metal nanowires of Au, Pt, and Pd.

In another approach, Cheon *et al.*[57] utilized vapor infiltration to synthesize Pd nanowires. An organometallic precursor was sublimed into the empty pores of MSNs and then pyrolyzed under an H_2 environment. In order to obtain unsupported Pd nanowires, the siliceous Pd composites were treated with an aqueous solution of hydrofluoric acid and XPS confirmed there were no palladium silicides present.

The methods used to synthesize metal nanorods in MSNs often result in a wide variation of nanorod lengths and incomplete pore filling. In one of the cases presented above (*i.e.* incipient wetness impregnation), capillary force drives the aqueous metal salt solution into the pores and complete pore filling during immersion is likely. However, the amount of solid occupying the pore space is limited by the solubility of the precursor in solution. Upon drying, the solubility limitations result in incomplete pore filling and lack of aspect ratio control in the final product (Figure 6).[58] In addition, even if a method was developed to allow for complete pore filling, aspect ratios below 50 would be difficult to achieve based on typical MSN dimensions (pore length and diameter). Similarly, vapor infiltration methods rely on diffusion of the gaseous precursor into the channels of mesoporous silica. The process is slow and suffers from pore blockage, thus also resulting in incomplete pore filling and lack of aspect ratio control.

Silica nanocapsules are an emerging class of silica templates offering many advantages over MSNs. There has been significant progress in the fabrication of well-defined 1D silica nanocapsules over the past decade;[59] unfortunately, most of the methods are limited by the difficulties associated with obtaining 1D templates of high quality and in large quantity. Very recently, Yin *et al.*[38] established a robust method for the synthesis of silica nanocapsules with precise aspect ratio control on the gram-scale by

templating against 1D nanocrystals. Crystalline nanorods of a nickel-hydrazine complex were first formed in reverse microemulsion by ligand-mediated preferential growth of certain facets. Following silica coating, selective etching of the nickel-hydrazine complex gave rise to silica nanocapsules of high uniformity and yield. The inner length of the silica nanocapsules can be tuned by varying the nickel concentration, while their inner diameter can be tuned by choosing different surfactants. The persistent problem of aspect ratio control and magnitude associated with MSN templates is alleviated by the nanocapsules prepared by the aforementioned procedure.
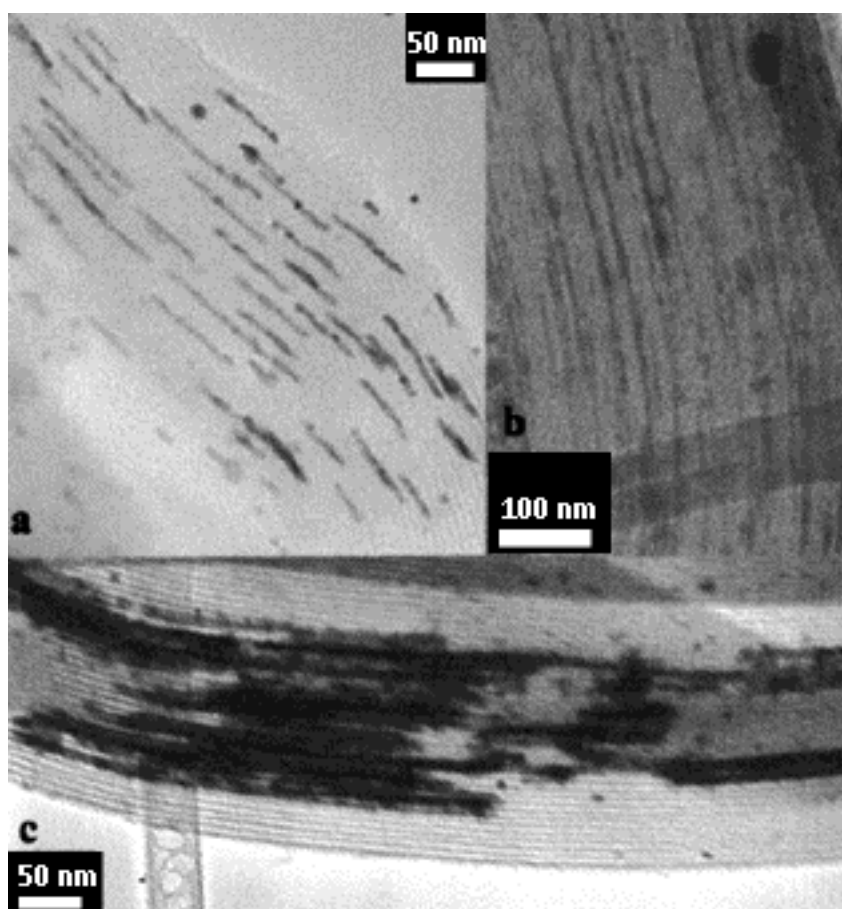
Figure 6. TEM micrographs of different metal nanowires grown within the framework of SBA-15: (a) Au/SBA-15; (b) Ag/SBA-15; (c) Pt/SBA-15.[58]

Template-directed synthesis of zero-valent metal nanorods offers increased advantages needed for the synthesis of bimetallic heterostructures compared to other commonly employed methods of nanorod synthesis. Utilizing discrete mesoporous silica templates results in superior aspect ratio control, increased monodispersity, and allows for scalability. Discrete mesoporous silica nanocapsules are therefore best suited for the synthesis of metal nanorods because of their many highly desirable properties relative to other templates and silica materials. The consistent and possibly scalable production of silica nanocapsules with high uniformity and size tunability makes them promising templates for the preparation of well-defined zero-valent metal nanorods.

Results and Discussion

Synthesis of Ni⊂SiO$_2$

By reduction of previously reported tris (hydrazine) nickel (II) chloride coated with silica ([Ni(N$_2$H$_4$)$_3$]Cl$_2$⊂SiO$_2$) by sodium borohydride (NaBH$_4$), followed by calcination under an H$_2$ atmosphere, we synthesized zero-valent nickel nanoparticles templated by amorphous silica (Ni⊂SiO$_2$) (Figure 7a and 7b).Powder X-ray diffraction (XRD), Fourier transform infrared spectroscopy (FTIR), high-resolution (HR) transmission electron microscopy (TEM), and energy-dispersive X-ray spectroscopy (EDX) showed that zero-valent nickel nanoparticles (Ni^0) are templated by amorphous silica. The structures display strong magnetic behavior at room temperature and preliminary data suggests Ni^0 particle size can be tuned while maintaining nanocapsule dimensions.
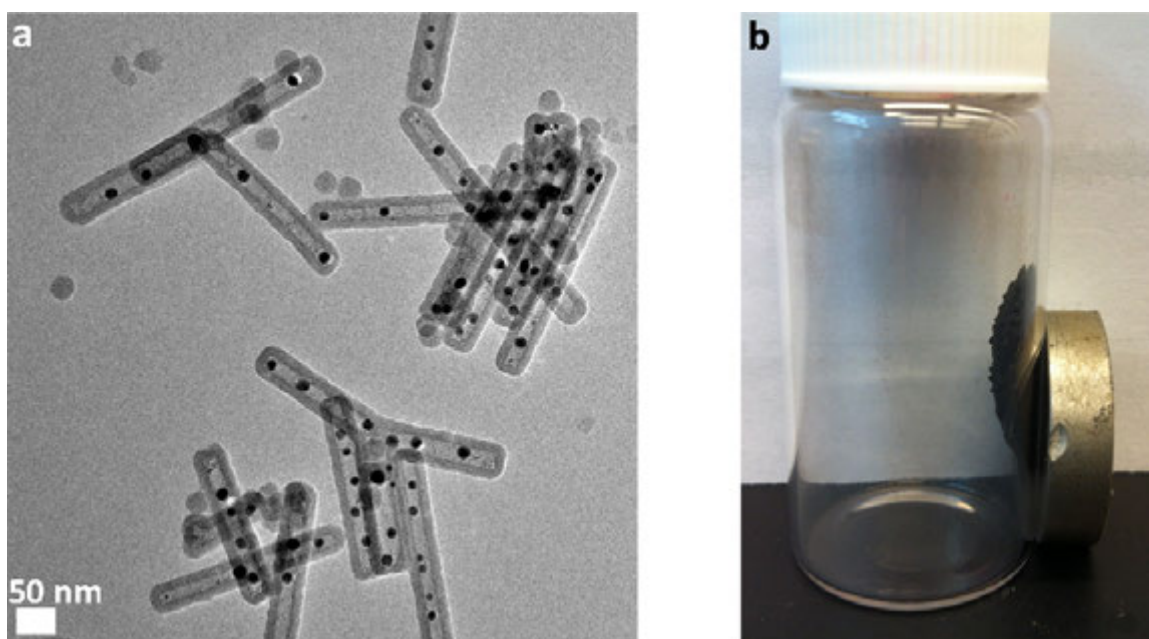
Figure 7. (a) TEM micrograph of Ni⊂SiO$_2$, and (b) Photograph showing its magnetic behavior.

Synthesis of the initial [Ni(N$_2$H$_4$)$_3$]Cl$_2$⊂SiO$_2$ core-shell complex was carried out in a water-in-oil reverse microemulsion.[38] Aqueous nickel (II) chloride hexahydrate (NiCl$_2$•6H$_2$O) constituted the dispersed phase, cyclohexane the continuous phase, and polyoxyethylene (20) cetyl ether (Brij58) was used as the surfactant. After mixing, a homogenized solution was obtained and hydrazine hydrate (N$_2$H$_4$•H$_2$O) was added in excess. Hydrazine is thought to coordinate to nickel centers to form a one-dimensional tris(hydrazine) nickel (II) chloride ([Ni(N$_2$H$_4$)$_3$]Cl$_2$) complex under these conditions. The 1D morphology was confirmed by scanning electron microscopy (SEM) (Figure 8a), and the complex was identified by its characteristic, previously reported XRD pattern (Figure 8b). Encapsulation by amorphous silica (Figure 8c) was obtained through *in-situ* introduction of tetraethylorthosilicate (TEOS) which easily undergoes hydrolysis and condensation catalyzed by diethylamine to yield amorphous silica. The diffraction pattern

(Figure 8d) clearly shows crystalline $[Ni(N_2H_4)_3]Cl_2$ is present after silica coating in addition to amorphous material centered around $2\Theta = 24°$.
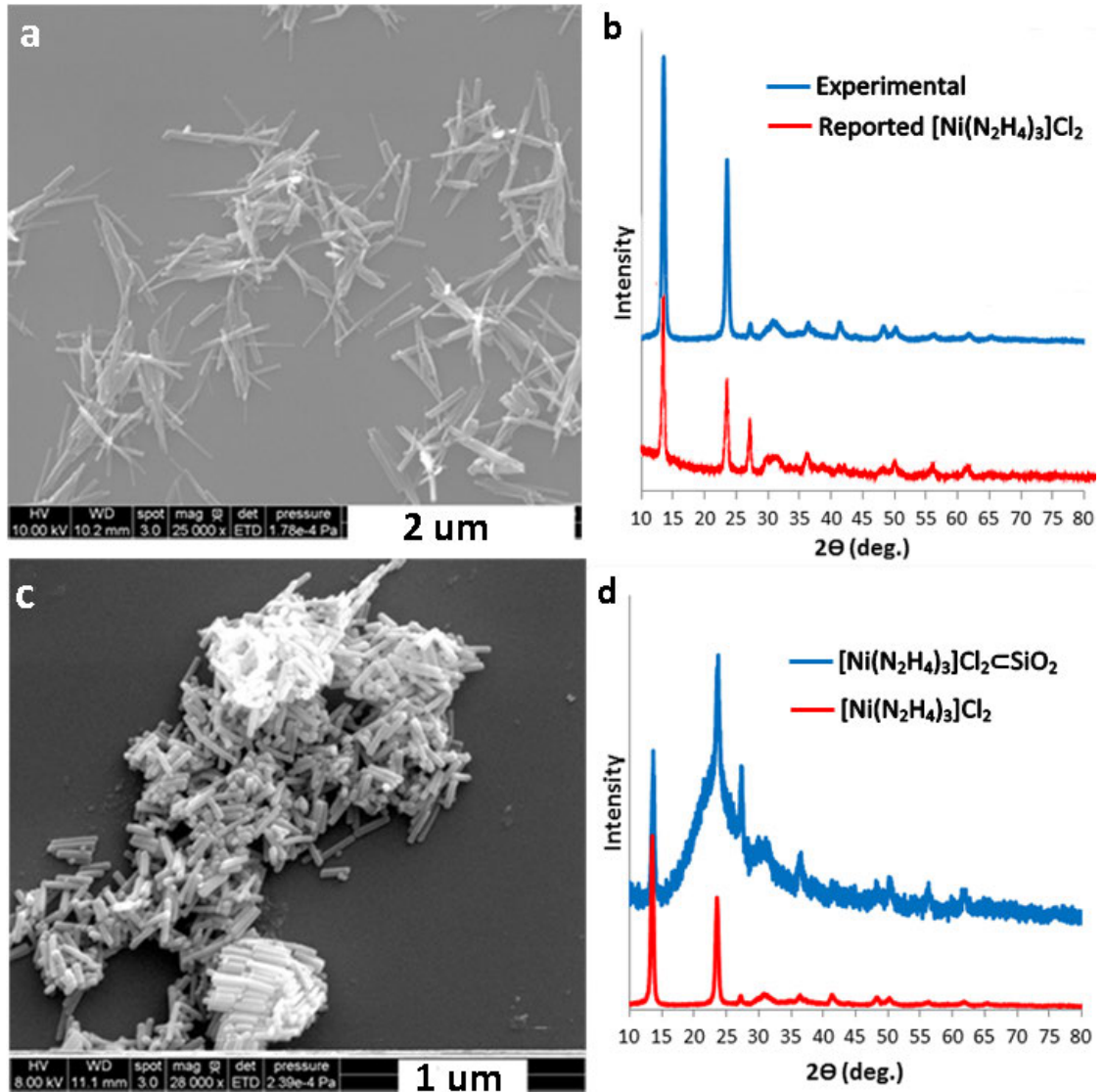
Figure 8. (a) SEM micrograph of $[Ni(N_2H_4)_3]Cl_2$ prepared by reverse microemulsion; (b) XRD pattern of experimental and $[Ni(N_2H_4)_3]Cl_2$ reference;[60] (c) SEM micrograph of $[Ni(N_2H_4)_3]Cl_2{\subset}SiO_2$; (d) XRD pattern of $[Ni(N_2H_4)_3]Cl_2{\subset}SiO_2$ and $[Ni(N_2H_4)_3]Cl_2$.

FTIR can be used to detect the presence of N_2H_4 ligands and the SiO_2 shell (Figure 9). The N-H symmetric stretching vibrations at 3213 cm^{-1} and 3156 cm^{-1}, and the

NH$_2$ bending and wagging between 1628-1192 cm^{-1} confirm the presence of hydrazine ligands in both [Ni(N$_2$H$_4$)$_3$]Cl$_2$ and [Ni(N$_2$H$_4$)$_3$]Cl$_2$⊂SiO$_2$.[61] The IR spectrum for [Ni(N$_2$H$_4$)$_3$]Cl$_2$⊂SiO$_2$ shows a strong, broad peak at 1190 cm^{-1} and 1090 cm^{-1} attributed to the longitudinal-optical (LO) and transverse-optical (TO) mode of Si-O-Si asymmetric bond stretching vibration, respectively.[62] The peaks present at 801 cm^{-1} and 461 cm^{-1} correspond to Si-O-Si symmetric stretching and bond bending vibrations, respectively.[62] Furthermore, the N-N stretching frequency reveals the binding mode of the hydrazine ligands to the metal center. The N-N stretching frequency of MCl$_2$(N$_2$H$_4$)$_2$ (M = Mn, Fe, Co, Ni, Cu, Zn, and Cd) was previously identified using isotopic labeling and found to lie in the range of 960-985 cm^{-1}.[63] These compounds are isomorphous and characterized by a polymeric structure of bridging bidentate ligands (-M(N$_2$H$_4$)$_2$M-); complexes containing unidentate ligands are expected to have decreased N-N stretching frequencies due to their less rigid environment. In 1968, Nicholls *et al.*[64] synthesized and characterized various cobalt-hydrazine complexes, and by comparing the N-N stretching frequencies of unidentate hydrazine [Co(N$_2$H$_4$)$_6$]Cl$_2$ (ν(N-N) = 928 cm^{-1}) and bidentate hydrazine [Co(N$_2$H$_4$)$_2$]Cl$_2$ (ν(N-N) = 970 cm^{-1}), they confirmed that bidentate hydrazine ligands are blue-shifted relative to unidentate hydrazine ligands. The [Ni(N$_2$H$_4$)$_3$]Cl$_2$ spectrum clearly shows a peak at 972 cm^{-1} and can thus be attributed to N-N stretching of the hydrazine ligands, suggesting the complex contains bidentate hydrazine ligands. Furthermore, due to the thermal stability and insolubility of [Ni(N$_2$H$_4$)$_3$]Cl$_2$, the hydrazine ligands are believed to be bridging bidentate rather than chelating bidentate. A proposed coordination environment consistent with the above information is shown in as an inset of Figure 9.
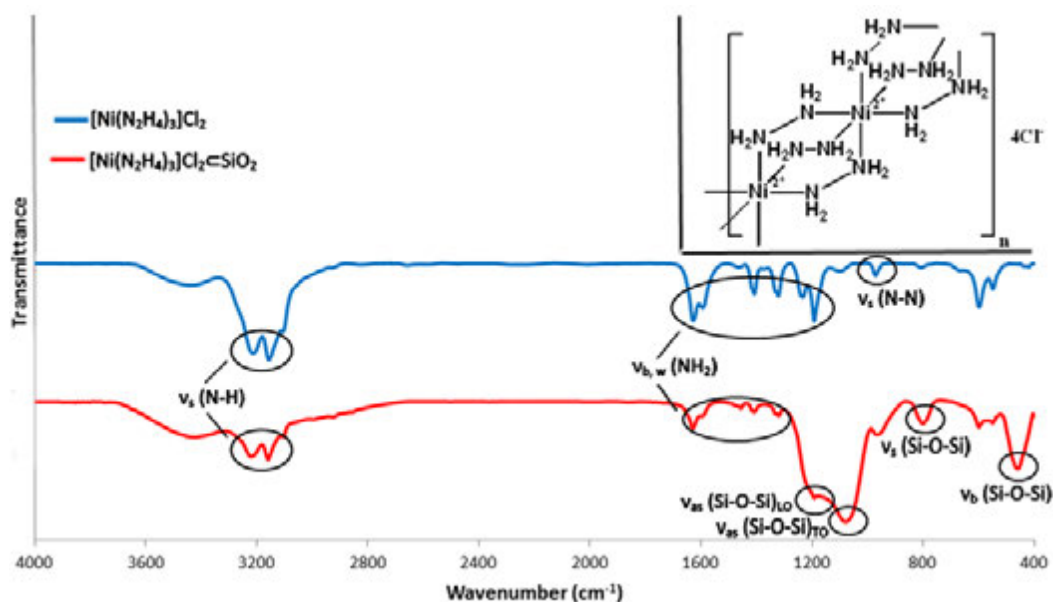
Figure 9. FTIR spectrum for $[Ni(N_2H_4)_3]Cl_2$ and $[Ni(N_2H_4)_3]Cl_2 \subset SiO_2$. Inset shows proposed Ni^{2+} coordination environment.

When $[Ni(N_2H_4)_3]Cl_2 \subset SiO_2$ is treated with hydrochloric acid (HCl), the silica shell is retained while the tris(hydrazine) nickel (II) chloride core is selectivity etched away giving rise to amorphous silica 1D templates.[38] The TEM micrograph (Figure 10a) confirms the templates have nanocapsule morphology. The thickness of the silica walls depends on the amount of TEOS used, in addition to the time used for hydrolysis and condensation reactions. Typical wall thicknesses are 15-20 nm under the conditions and times used. The FTIR spectrum (Figure 10b) confirms that hydrazine ligands are no longer present after acid etching evidenced by the lack of bands at 3213 cm^{-1} and 3156 cm^{-1}. The post-etch spectrum shows peaks at 2849 cm^{-1} and 2919 cm^{-1} which are characteristic of C-H stretching and can be attributed to incomplete removal of Brij 58 surfactant. The diffractogram (Figure 10c) shows that after treatment of $[Ni(N_2H_4)_3]Cl_2 \subset SiO_2$ with HCl, crystalline material is no longer present.
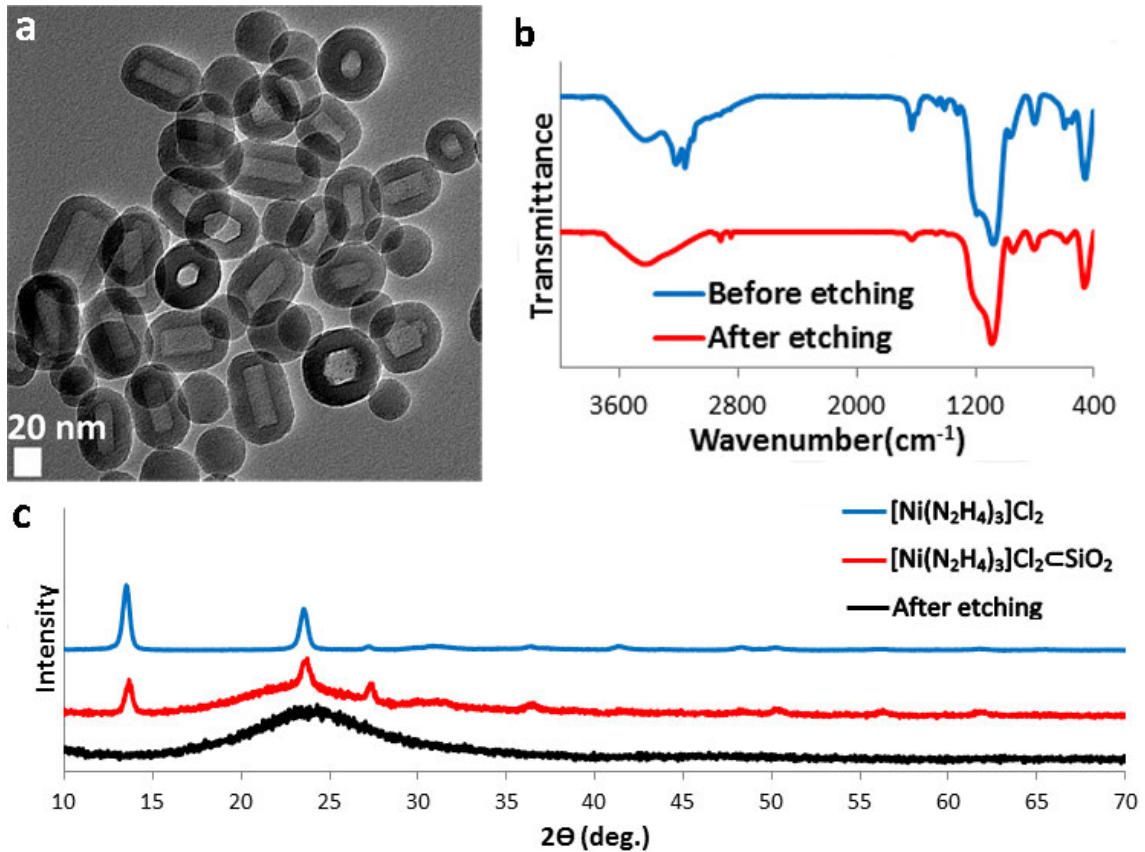
Figure 10. (a) TEM micrograph of silica nanocapsules; (b) FTIR spectrum before and after HCl etching $[Ni(N_2H_4)_3]Cl_2 \subset SiO_2$; (c) XRD data of $[Ni(N_2H_4)_3]Cl_2$, $[Ni(N_2H_4)_3]Cl_2 \subset SiO_2$, and after etching with HCl (*i.e.* silica nanocapsules).

Using different amounts of aqueous $NiCl_2 \cdot 6H_2O$ while keeping the amount of Brij 58 and hydrazine constant allows the isolation of nanocapsules with different lengths (Figure 11a-d).[38] The width of the nanocapsules in all experiments (40-70 nm) is constant and dependent on the length of the polar polyoxyethylene chain of the surfactant used in their synthesis.[38] To demonstrate the degree of aspect ratio control that can be achieved by this method, we plotted the average nanocapsule length versus the amount of $[NiCl_2 \cdot 6H_2O]$ used (Figure 11e). The SEM micrographs, histogram, and plot clearly show that nanocapsule aspect ratio can be precisely controlled and easily predicted. The

deviation in nanocapsule lengths increases when [NiCl$_2$•6H$_2$O] is greater than 1.1 mM compared to when the ratio is less than 0.8 mM.
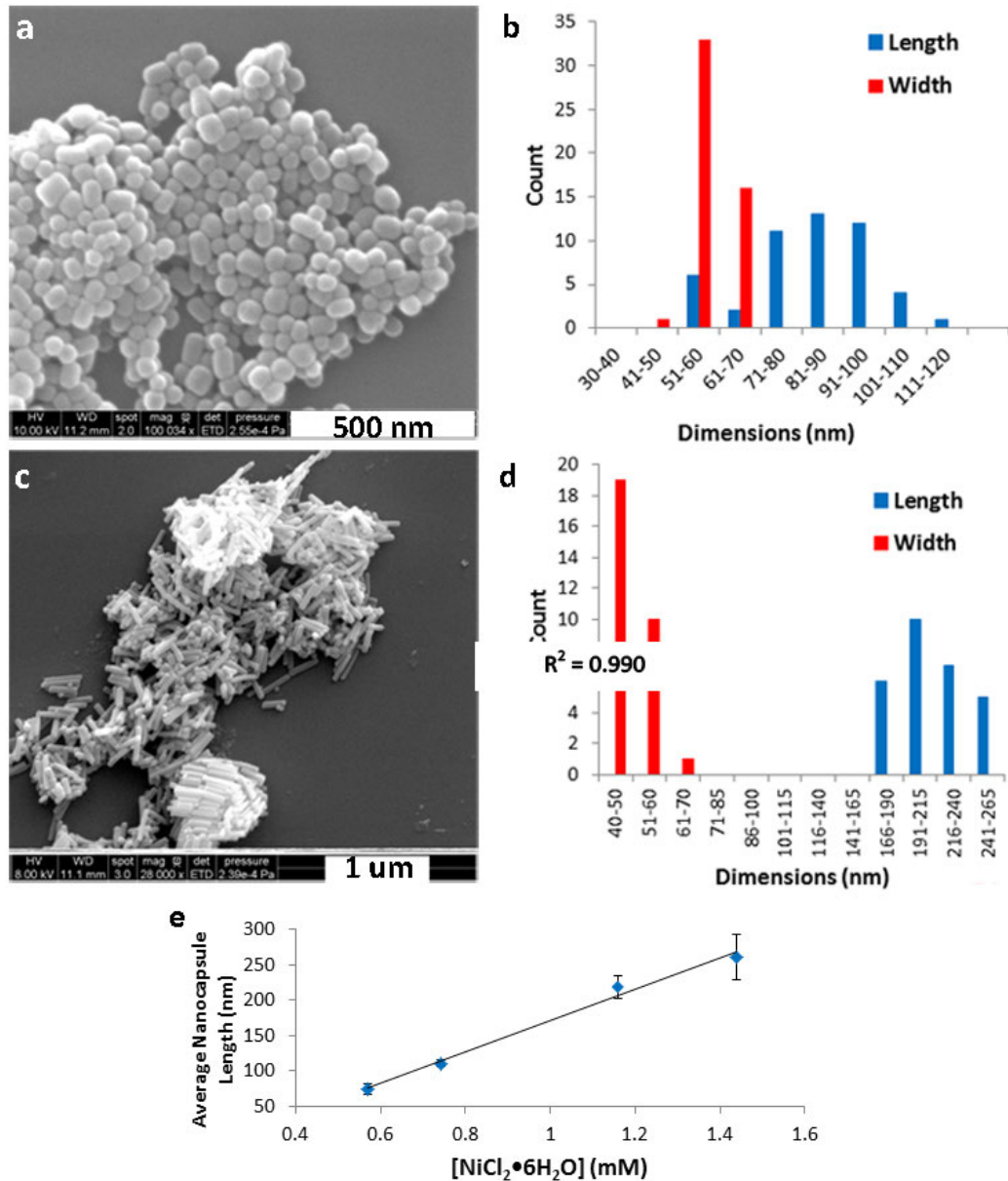
**Figure 11.** (a) and (c) SEM micrographs of silica nanocapsules prepared with different amounts of NiCl$_2$; (b) and (d) Size histogram of silica nanocapsules corresponding to (a) and (c), respectively.(e) Plot of silica nanocapsule length versus [NiCl$_2$•6H$_2$O]. A linear regression line was used to fit the set of data points. The coefficient of determination is shown in the lower right of the plot area. The error bars represent one standard deviation from the mean.

To synthesize zerovalent metal nanorods, we first explored the chemical conversion (reduction) of surfactant-stabilized tris(hydrazine) nickel (II) chloride to nickel metal. Nickel metal is fairly active and, if successful, could lead to indirect synthesis of other catalytic (dehydrogenation/ hydrogenation) metals (Pd, Pt, Rh, Ru, Ir) through galvanic exchange. The most notable colloidal synthesis of nickel nanorods has been demonstrated through thermal decomposition of nickelocene in the presence of hexadecylamine (HDA).[65] Unfortunately, the cost of nickelocene precursor is too high for scalable synthesis, and therefore this method is not ideal for the synthesis of metal nanorods for use in bimetallic heterostructures. Other methods of synthesis include a polyol process,[66] solvothermal decomposition of nickel acetate (Ni(CH$_3$COO)$_2$,[67] and reduction of NiCl$_2$ by hydrazine in a reverse water/butanol/potassium oleate/kerosene microemulsion.[68] However, these methods are fraught with wide polydispersities and lack of aspect ratio control or well-defined morphologies.

Hydrazine is a powerful reducing agent when present in alkaline environments (Scheme 3a) and is capable of reducing Ni^{2+} (Scheme 3b).[60] Reduction of [Ni(N$_2$H$_4$)$_3$]Cl$_2$ complex by introduction of hydroxide ($^-$OH) ion has been reported for the synthesis of nickel powders.[60] Given the 1D morphology of the [Ni(N$_2$H$_4$)$_3$]Cl$_2$ complex formed by reverse microemulsion, introduction of hydroxide ion could result in reduction while maintaining morphology. Literature XRD analysis suggests that reduction of [Ni(N$_2$H$_4$)$_3$]Cl$_2$ complex by addition of hydroxide ion proceeds through a nickel hydroxide (Ni(OH)$_2$) intermediate.[60] Reduction of Ni(OH)$_2$ is then accomplished through the combination of half-cell reactions shown in Scheme 3a and 3b. *In-situ* addition of sodium hydroxide (NaOH) after reverse microemulsion formation of [Ni(N$_2$H$_4$)$_3$]Cl$_2$

complex resulted in face-centered cubic nickel (fcc-Ni^0), as confirmed by its XRD pattern (Figure 12a). However, the TEM micrograph (Figure 12b) shows only a fraction of the product is present with the desired morphology, albeit this fractions ill-defined; most of the product was present as large spherical agglomerates. Clearly, introduction of NaOH did not preferentially maintain the 1D morphology upon conversion of $[Ni(N_2H_4)_3]Cl_2$ complex to Ni^0, possibly due to the uncontrolled rate of NaOH addition or the inefficient ligand stabilization of the $Ni(OH)_2$ intermediate and/or product that was shown to be present in this reaction.[60] Better control over the rate of NaOH addition may be needed in order to obtain the desired 1D Ni^0morphology. Additional experiments may be necessary in order to determine what is (are) the best surfactant(s) required to effectively stabilize a preferential amount of the product exhibiting 1D morphology.
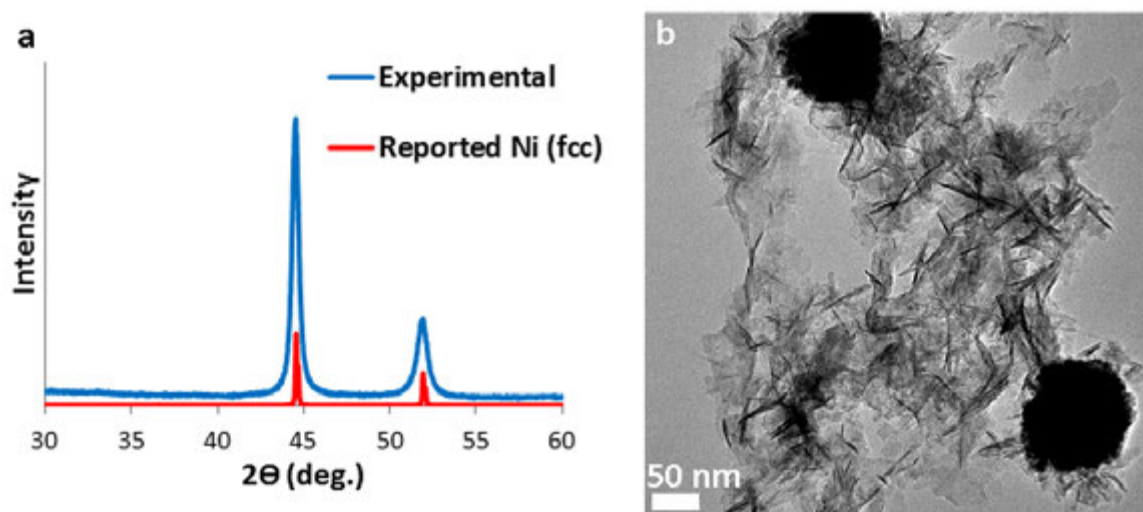
Figure 12. (a) XRD pattern and (b) representative TEM micrograph of the product obtained from *in-situ* addition of NaOH to $[Ni(N_2H_4)_3]Cl_2$ in reverse microemulsion.
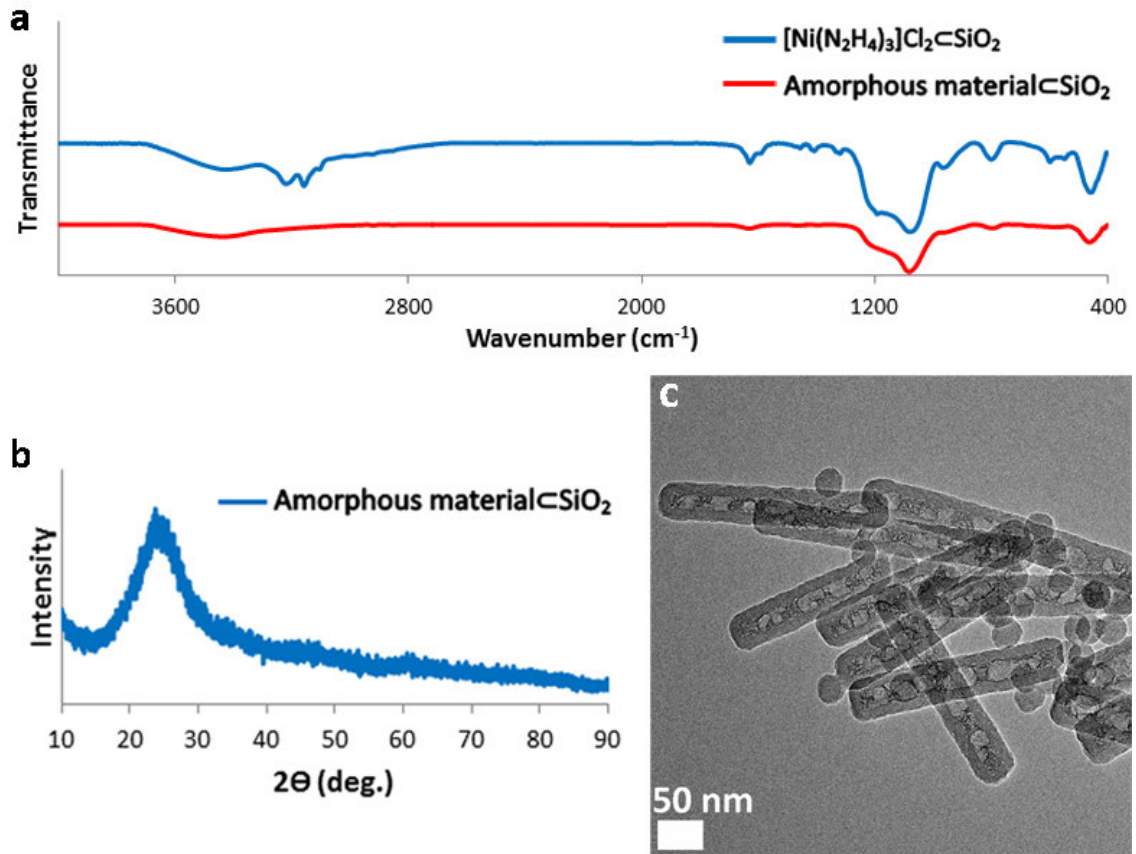
Scheme 3.

(a) $N_2H_4 + 4^-OH \longrightarrow N_2 + 4H_2O + 4e^-$ $E^° = -1.16$ V

(b) $Ni^{2+} + 2e^- \longrightarrow Ni^0$ $E^° = -0.76$ V
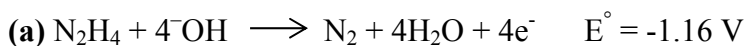
The next approach we explored to obtain 1D Ni^0 materials was chemical

reduction of $[Ni(N_2H_4)_3]Cl_2 \subset SiO_2$ with $NaBH_4$. Briefly, $[Ni(N_2H_4)_3]Cl_2 \subset SiO_2$ was

suspended in H_2O and while stirring, an aqueous solution of $NaBH_4$ was added dropwise.

Upon addition of $NaBH_4$, the suspension immediately underwent a color change from

pink to black, with the evolution of copious amounts of gas. The FTIR spectrum (Figure

13a) of the product (amorphous material$\subset SiO_2$) confirms hydrazine ligands are no longer

present, and the diffractogram (Figure 13b) shows no crystalline material. TEM (Figure

13c) shows varying degrees of contrast along the length of the nanocapsule cavity,

suggesting there is material within the nanocapsule cavity, but the methods employed are

unable to afford unambiguous characterization.

It is well established that reacting aqueous nickel salts with sodium borohydride

produces nickel/nickel boride (Ni^0/Ni_xB_y) amorphous materials[69,70,71] (Scheme 4a-c), but

the mechanism by which Ni_xB_y is formed remains unknown.[72] The stoichiometry of the

final compound (values of "x" and "y") obtained upon crystallization depend on the

amount of boron in the amorphous material. Crystallization of Ni^0/Ni_xB_y is achieved

through thermal treatment under inert atmosphere and post-heating (500°C) XRD

analysis has shown fcc-Ni is the major product.[73] Thus, thermal treatment of amorphous

material$\subset SiO_2$ from room temperature to 500°C under Argon (Ar) was utilized to form

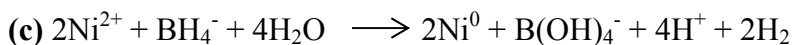crystalline Ni^0. However, the XRD pattern (Figure 14) shows rock-salt nickel oxide
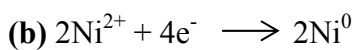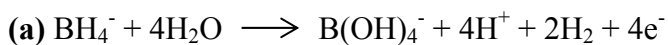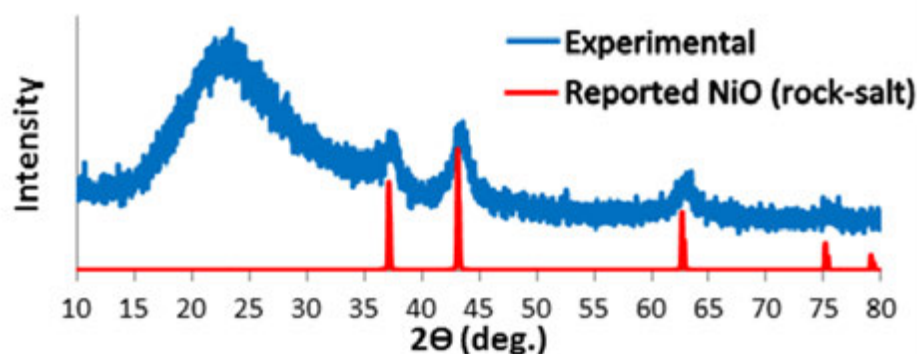
(NiO) is the prevalent phase and an average crystallite size of 5.3 nm was found using the Scherrer equation. TEM analysis (Figure 18a and 18b) shows the average particle size (4.9 ± 2.0 nm) is in good agreement with XRD data.

Figure 13. (a) XRD data, (b) FTIR spectrum, and (c) TEM micrograph of amorphous material⊂SiO_2.

Scheme 4.

(a) $BH_4^- + 4H_2O \longrightarrow B(OH)_4^- + 4H^+ + 2H_2 + 4e^-$

(b) $2Ni^{2+} + 4e^- \longrightarrow 2Ni^0$

_____

(c) $2Ni^{2+} + BH_4^- + 4H_2O \longrightarrow 2Ni^0 + B(OH)_4^- + 4H^+ + 2H_2$

Figure 14. XRD pattern after thermal treatment of amorphous material$\subset$SiO$_2$.

Silica is known to absorb water within the Si-O-Si matrix and silanol (Si-OH) groups undergo dehydration to yield siloxanes at elevated temperatures which are possible sources of oxygen giving rise to NiO$\subset$SiO$_2$.[74] Silanol dehydration was confirmed by comparing the FTIR spectrum (Figure 15a) of as-synthesized and calcined silica (*as*-SiO$_2$ and *c*-SiO$_2$, respectively). The spectrum clearly shows the Si-OH stretching frequency is present at 947 cm^{-1} in *as*-SiO$_2$, but upon calcination at 500°C, the Si-OH stretching frequency is no longer present in *c*-SiO$_2$. To test this idea, the heating procedure was repeated without the silica shell. A [Ni(N$_2$H$_4$)$_3$]Cl$_2$ aqueous suspension was treated with aqueous NaBH$_4$ and the resulting as-synthesized material was calcined under Ar flow at 500°C at a heating rate of 10°C min^{-1}. Indeed, calcination in this case resulted in nearly phase pure fcc-Ni as shown by the XRD pattern (Figure 15b). There is also peaks attributed to rock-salt NiO and could be due to the relatively high ramp rate used in the synthesis not allowing adequate time for the sample to dry before reaching oxidation temperatures. X'Pert HighScore Plus structural refinement shows the material consists of about 95 % Ni and 5% NiO.
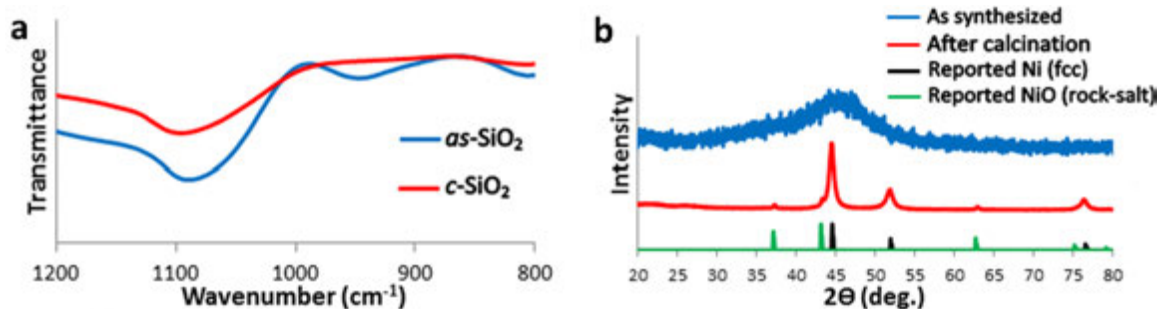
Figure 15. (a) FTIR spectrum of showing dehydration of Si-OH groups (947 cm^{-1}) upon calcination; (b) XRD pattern showing amorphous material and its calcination products.

In order to circumvent nickel oxidation in the presence of silica during calcination, the reaction was run under a flow of Ar/H$_2$ while keeping all other conditions identical. In this case, the XRD pattern of the product (Figure 16a) shows fcc-Ni^0 with an average crystallite size of 12 nm estimated using the Scherrer equation and is in good agreement with the average particle size (13.7 ± 3.5 nm) obtained from TEM analysis (Figure 16c, 16d, 16e, and 16f). An EDX line scan was used to confirm the particles contained nickel. Weight percent nickel versus length along the rod (red line) is plotted (Figure 16b) for the micrograph shown to the right of the plot. Areas of high contrast correspond to high nickel X-ray intensities and areas of low contrast correspond to low nickel X-ray intensities providing strong evidence that nickel particles are contained within the silica nanocapsule. HR-TEM micrographs (Figure 16e) were taken and fast Fourier transform analysis resulted in observed *d*-spacings corresponding to (111) and (200) planes of fcc-Ni. Also observed where the (111) and (200) planes from rock-salt NiO. It is common to have a thin oxide layer present on the surface of nickel. The thin oxide layer helps passivate and protect Ni, making it relatively inert towards further oxidation at ambient temperature and pressure. The average number of particles per rod is

4 ± 2 (Figure 16g) and these are dispersed within the oxide support. Only about 1% of the

capsules were found to be void of particles.
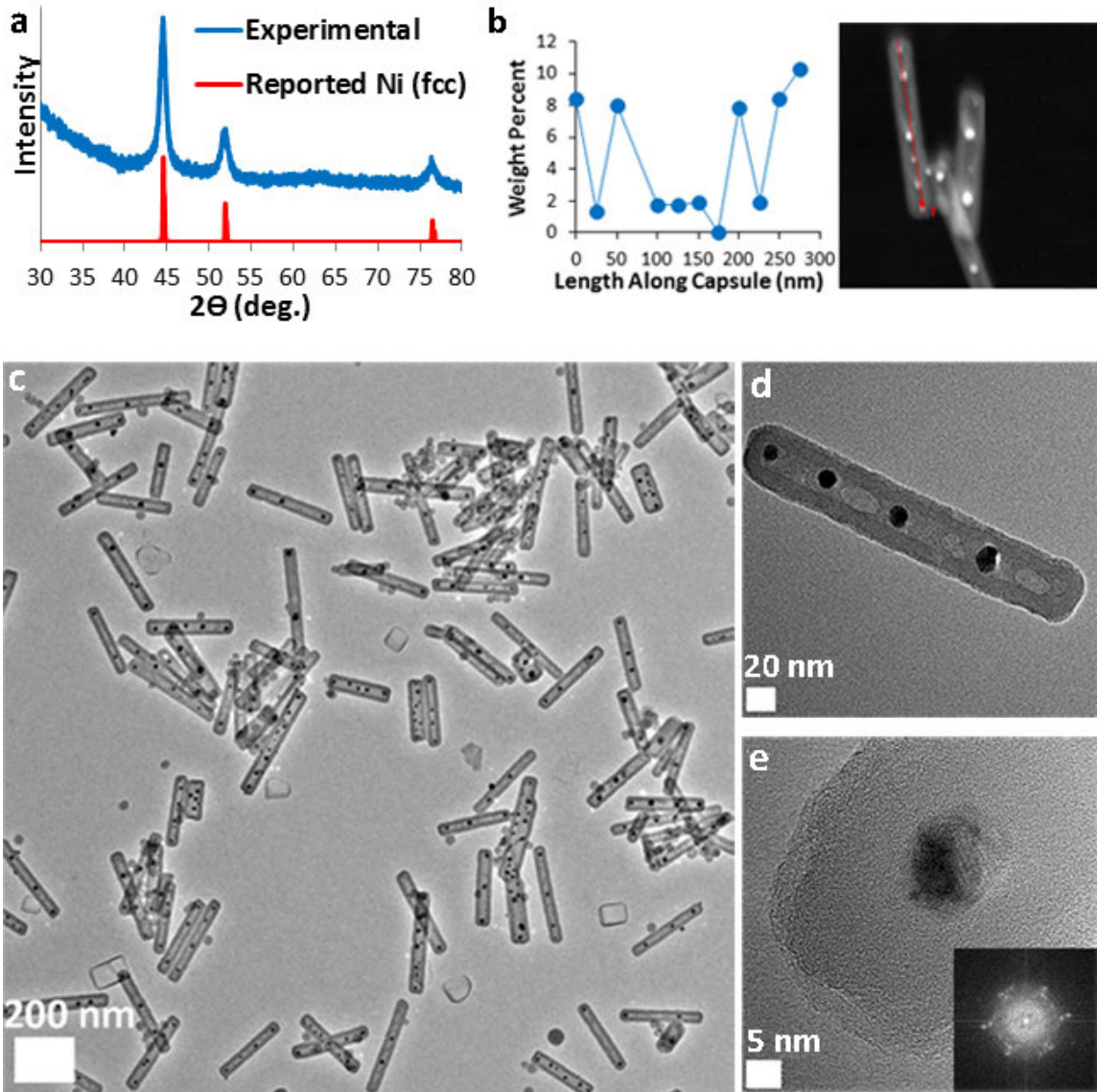

Figure 16. (a) XRD pattern of Ni⊂SiO$_2$; (b) Plot of weight percent nickel *vs.* length along rod from EDX data; (c) and (d) TEM micrograph of Ni⊂SiO$_2$; (e) HRTEM micrograph and corresponding electron diffraction pattern for Ni⊂SiO$_2$.
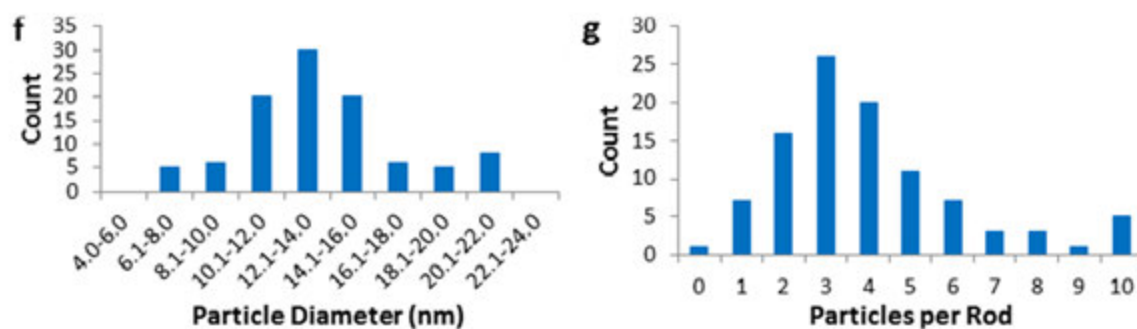
Figure 16 (continued). (f) Histogram showing particle size distribution; (g) Histogram showing number of particles per rod.

As previously mentioned, the reaction between $[Ni(N_2H_4)_3]Cl_2$ and $NaBH_4$ is expected to produce amorphous nickel boride (Ni-B). To probe the possible presence of Ni-B, a sample obtained from treating $[Ni(N_2H_4)_3]Cl_2$ with $NaBH_4$ was studied by hot-stage (variable temperature) XRD (Figure 17). The obtained diffractograms clearly show the amorphous material undergoing structural changes to yield fcc-Ni. At 275°C, the diffraction pattern shows the emergence of peaks not attributable to fcc-Ni. The peaks become even more pronounced at 300°C and eventually disappear at 350°C. The additional peaks observed in the diffraction pattern obtained upon calcination at 300°C match relatively well and may be due to orthorhombic nickel boride (Ni_3B). General Structure Analysis System (GSAS) structural refinement shows the material consists of about 91 % Ni and 9% Ni_3B. The slight observed shift to lower two-theta angle relative to the standard pattern may be due to thermal expansion of the lattice at the temperature used to collect the XRD. The shift to lower two-theta values is also demonstrated by observing the XRD patterns at 350°C and 400°C compared to the fcc-Ni standard pattern and the XRD pattern of the calcined product at 35°C. It is clear that any Ni_3B phase has completely decomposed at 400°C, but the decomposition product is not known. Previous

XPS analyses on amorphous Ni-B materials show the presence of oxidized and reduced boron species identified as boron trioxide (B_2O_3) and Ni_xB_y, respectively.[73, 75,76] Upon heat treatment of Ni-B materials under inert atmosphere, XPS analysis showed the disappearance of reduced boron and the enhancement of oxidized boron.[73] It is unlikely that the intermediate Ni_3B phase undergoes gaseous decomposition due to the high boiling points of the constituents, but transforms instead to an amorphous form of the most stable oxide of boron (B_2O_3). B_2O_3 is extremely difficult to crystallize under ambient pressures and this could be the reason why this phase is not detected using XRD analysis.[77]. Further elemental analysis and XPS studies may be necessary to fully establish the fate of the Ni_3B phase.
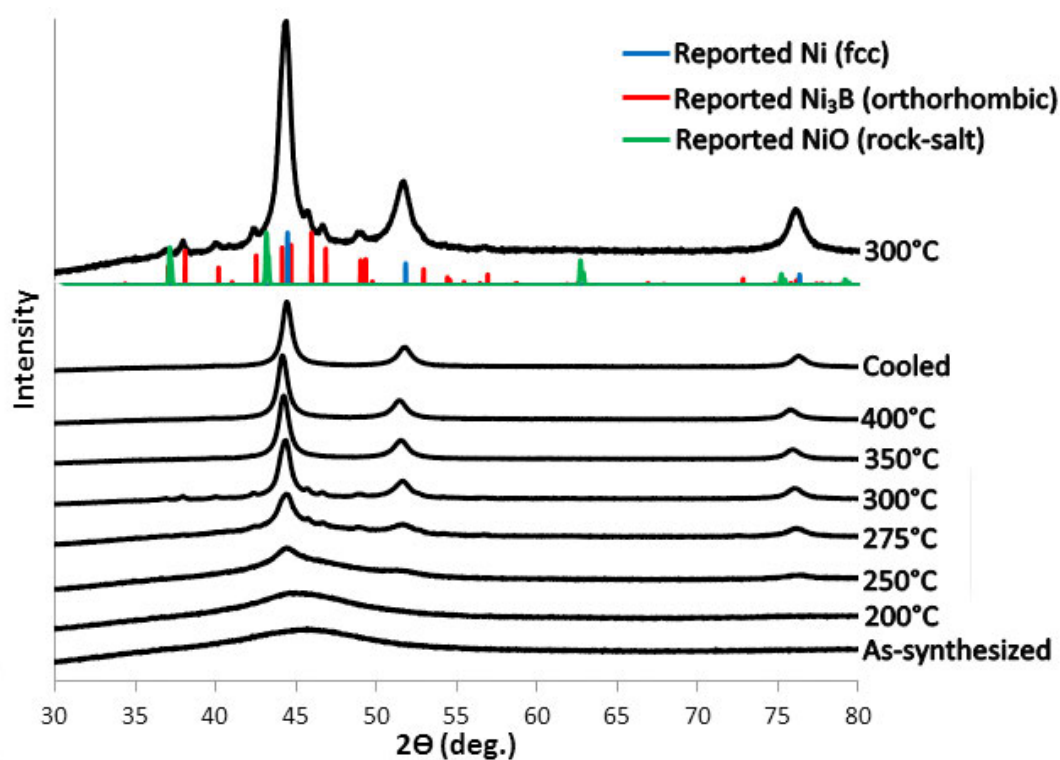
Figure 17. *In-situ* XRD data for product obtained from reaction of [Ni(N$_2$H$_4$)$_3$]Cl with NaBH$_4$ as a function of temperature. Heating rate 5°C min^{-1}.

It is interesting to note that the Ni^0 particle sizes obtained by calcination under Ar/H$_2$ are significantly larger than the NiO particle sizes obtained by calcination under Ar (Figure 18a and 18b). This observation can be explained by particle-support interactions; nickel oxides interact more strongly with oxide supports than nickel metal, thus resulting in less particle mobility and sintering (*i.e.* smaller particles) for NiO⊂SiO$_2$.[78] TEM micrographs show NiO particles spread on the surface of silica more than Ni^0 particles possibly due to the increased particle-support interaction and the spreading results in smaller, less uniform particle diameters for NiO compared to Ni^0. In summary, conversion of the amorphous Ni-B intermediate to NiO or Ni^0 resulted in two different size particles, suggesting the observed Ni^0 particles are formed by a sintering mechanism. This will be discussed further in the following paragraphs.
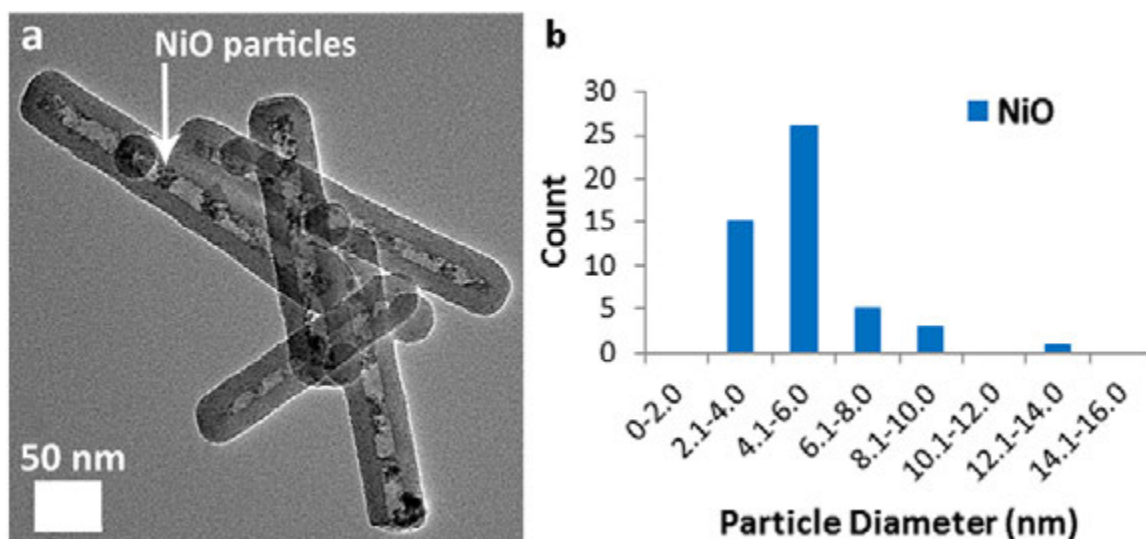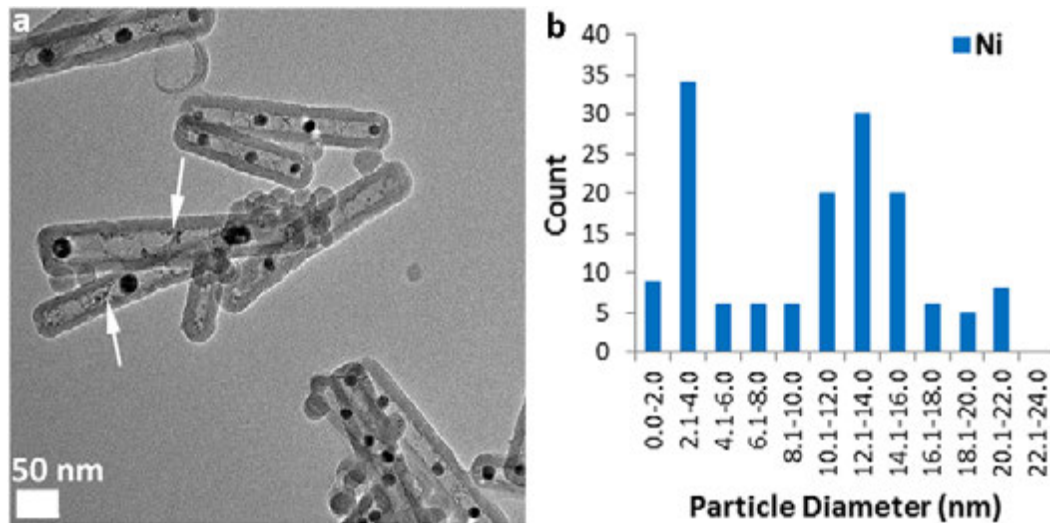

Figure 18 (a) TEM micrograph of NiO⊂SiO$_2$ obtained by calcination of Ni-B⊂SiO$_2$ under Ar atmosphere; (b) Particle size distribution histogram of NiO.

As observed by TEM, the $[Ni(N_2H_4)_3]Cl_2 \subset SiO_2$ materials possess relatively uniform contrast along the length of the nanocapsule interior, suggesting the nanocapsules are completely filled. This is consistent with the morphology of silica capsules after etching with HCl (Figure 10a). Upon treatment of $[Ni(N_2H_4)_3]Cl_2 \subset SiO_2$ with NaBH$_4$, TEM (Figure 13c) exhibits a difference in contrast along the length of the nanocapsules, suggesting they are no longer completely and uniformly filled; however, no discernible particles were observed by TEM. After NaBH$_4$ treatment, the product obtained has lost a significant amount of its original constituents (*i.e.* N$_2$H$_4$), as confirmed by FTIR analysis (Figure 13b). Thus, one should not expect complete filling of the nanocapsule interior. This could be the reason why rods are not formed during the subsequent calcination step and why there is clearly not enough Ni^0 inside the nanocapsule cavity to fill the entire void space.

Calcination of amorphous Ni-B$\subset$SiO$_2$ under H$_2$ resulted in spherically-shaped, crystalline fcc-Ni^0. Calcination of Ni-B$\subset$SiO$_2$ under Ar gave rise to NiO particles (average diameter = 4.9 nm) that exhibit smaller particle sizes and less shape uniformity compared to Ni^0 particles (average diameter = 13.7 nm). This suggests that during/after transformation from Ni-B$\subset$SiO$_2$ to Ni$\subset$SiO$_2$, the Ni^0 particles are able to sinter at higher rates relative to NiO particles, leading to the observed spherical and more regular morphology. The two mechanisms that have been proposed to explain sintering of supported Ni^0 are atomic migration (Ostwald ripening) and particle migration (coalescence). It has been shown that the mechanism of Ni^0 sintering on silica depends on the atmosphere used during calcination.[79,80] Under vacuum, Ni^0 particle sintering has been shown to occur through both mechanisms. However, under H$_2$ atmosphere, particle

migration is suppressed and atomic migration becomes the predominant mechanism attributed to increased interaction between the Ni^0 particle and the silica support, relative to vacuum. Upon closer examination of $Ni \subset SiO_2$ TEM micrographs (Figure 19a), there is a bimodal distribution of particle sizes (Figure 19b) supporting an atomic migration sintering mechanism and consistent with the aforementioned literature results. However, other factors that contribute to particle mobility including support porosity and surface impurities cannot be overlooked in the formation of spherical nickel particles.[78]

Figure 19. (a) TEM micrograph of $Ni \subset SiO_2$ showing different size particles obtained by calcination of $Ni-B \subset SiO_2$ under H_2 atmosphere; (b) Particle size distribution histogram of Ni^0 showing bimodal distribution.

Preliminary data suggests we are able to control Ni^0 particle size while maintaining nanocapsule dimensions by varying the amount of aqueous $NiCl_2$ used in the synthesis and keeping the surfactant to water ratio constant. The $[Brij\ 58]:[NiCl_2]$ ratio was held constant at 5.0 and different amounts of aqueous $NiCl_2$ were added into the

system (9.27 mmol of hydrazine hydrate was used in both experiments). Plotting particle diameter and number of particles per capsule versus concentration of $NiCl_2$ (Figure 20c) and nanocapsule cavity dimensions versus concentration of $NiCl_2$ (Figure 20d) clearly shows the effect of adding $NiCl_2$ while keeping the same surfactant to water ratio. The plot in Figure 20c shows an increase in the amount of aqueous $NiCl_2$ results in an increase of average particle size and a small, perhaps statistically insignificant decrease in the average number of particles per rod. The latter observation suggests that the increase in particle size cannot be solely attributed to differences in sintering rates. Figure 20d shows that the cavity length did not change, which is not the case when the concentration of $NiCl_2$ is increased without keeping the same [Brij 58]:[$NiCl_2$] ratio (Figure 11). In conventional Ni/SiO_2 catalysts, it was found that Ni^{2+} precursor loading is proportional to Ni^0 particle size.[81] The observed increase in particle size for $Ni \subset SiO_2$ could be due to an increased amount of Ni^{2+} within the nanocapsule, resulting in slightly higher amounts of $[Ni(N_2H_4)_3]Cl_2$ within any given nanocapsule. Figure 20d shows a statistically significant increase in cavity diameter when the concentration of $NiCl_2$ is increased, suggesting there is an increased amount of $[Ni(N_2H_4)_3]Cl_2$ within the nanocapsule. If this is the case, the increased amount of Ni^{2+} upon reduction and calcination could result in the observed increase in particle size. More studies will be needed to confirm this hypothesis. Unfortunately, a similar paper was published in June 2012.[82]

The next approach used to synthesize Ni^0 nanorods was thermal decomposition of $[Ni(N_2H_4)_3]Cl_2 \subset SiO_2$ to $Ni \subset SiO_2$. $[Ni(N_2H_4)_3]Cl_2 \subset SiO_2$ powder was placed into a tube furnace and the temperature ramped up to 500°C at 10°C min^{-1} under Ar and Ar/H_2 atmospheres. TEM analysis of products obtained under Ar (Figure 21a) show 1D material

in the interior of the nanocapsule. However, there is a significant amount of capsules (*ca.* 75%) that show no contrast variation in their interior, leading us to think that a mobile species was present during the decomposition resulting in the diffusion of the material outside of the nanocapsule. The XRD pattern for the product obtained by decomposition of $[Ni(N_2H_4)_3]Cl_2 \subset SiO_2$ under Ar (Figure 21b) shows the presence of both fcc-Ni^0 as well as rock-salt NiO, the latter attributed to absorbed water within the silica matrix and dehydration of Si-OH groups. To circumvent $NiO \subset SiO_2$ as a product, decomposition was carried out under Ar/H_2 reducing environment. In this case, the XRD pattern (Figure 21d) shows the major product is fcc-Ni^0, but the TEM micrograph (Figure 21c) shows a minimal amount of capsules (*ca.* 23%) have material inside their cavity.
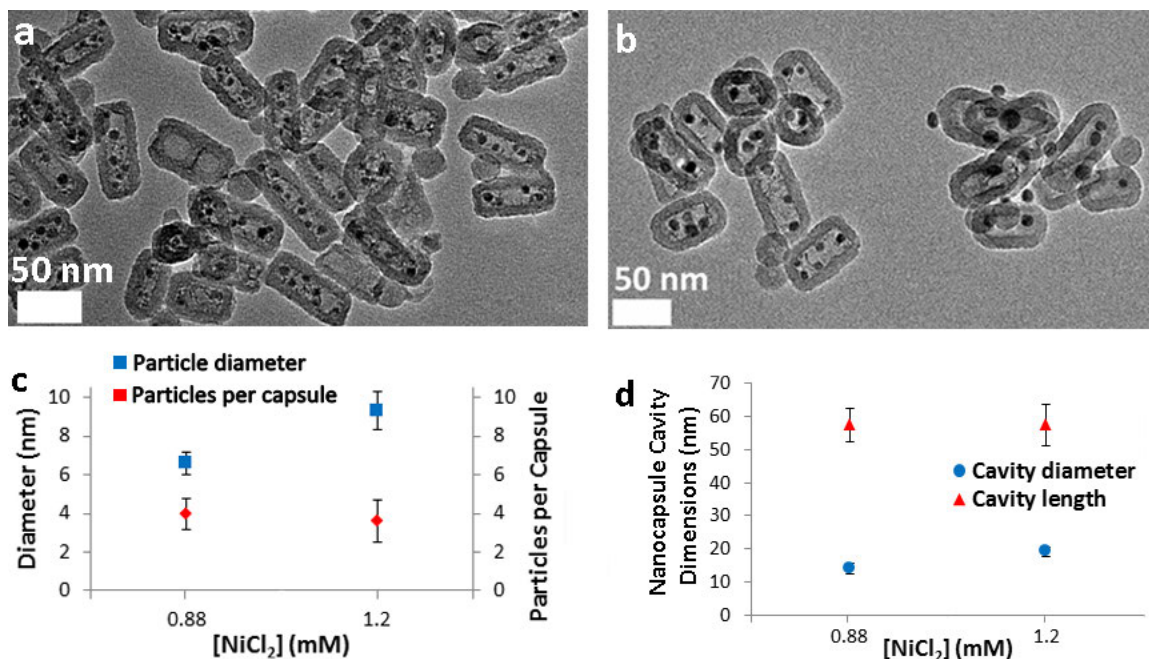

Figure 20. (a) TEM micrograph of $Ni \subset SiO_2$ using 0.88 mM $NiCl_2$; (b) TEM micrograph of $Ni \subset SiO_2$ using 1.2 mM $NiCl_2$; (c) Plot of particles per capsule and diameter versus $[NiCl_2]$; (d) Plot of average nanocapsule cavity dimensions versus $[NiCl_2]$. Error bars represent standard deviation from the mean.
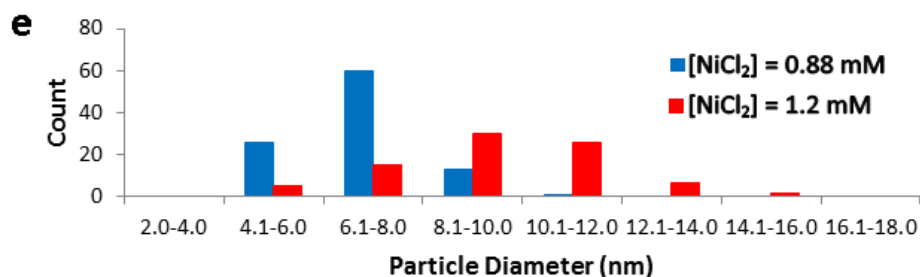
Figure 20 (continued). (e) Particle size distribution histogram corresponding to the TEM micrographs in (a) and (b).

Thermal treatment of metal-hydrazine complexes $[M(N_2H_4)_n]^{2+}$ (M = Mn, Fe, Co, Ni, Zn, and Cd, n = 2 or 3) in air is known to result in the loss of hydrazine followed by metal oxide formation at higher temperatures.[83] Hydrazine itself undergoes thermal decomposition to N_2 and NH_3 at 240°C.[84] Gaseous by-products from hydrazine decomposition during the thermal decomposition of $[Ni(N_2H_4)_3]Cl_2 \subset SiO_2$ under Ar/H_2 could explain why many capsules lack Ni metal. It has been shown that NH_3 and H_2 environments lead to substantially increased sintering rates (*i.e.* high particle mobility) during heat treatment of nickel particles on metal oxide surfaces compared to only NH_3, H_2, or NH_3/N_2 environments.[85] The hydrazine decomposition product of ammonia coupled with the hydrogen reducing environment could possibly lead to formation of mobile species that give rise to the observed diffusion and agglomeration of nickel outside of the nanocapsule cavity shown in Figure 21c. A similar argument can be made for the decomposition experiment under Ar, whereby the newly formed Ni^0 particles could act as a catalyst for the decomposition of NH_3 (from hydrazine ligand) to N_2 and H_2, thereby producing a NH_3/H_2 environment.
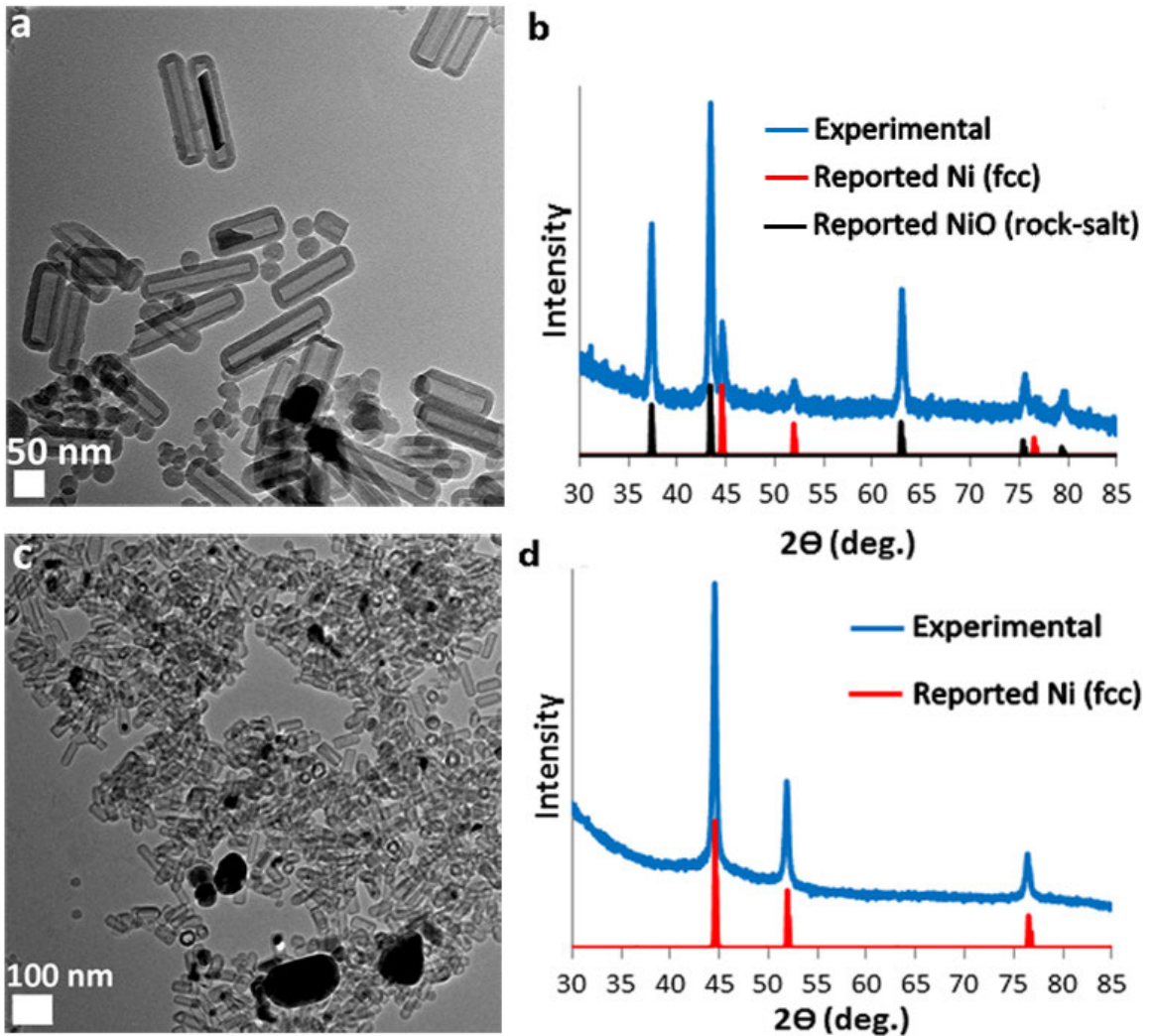
Figure 21. (a) TEM and (b) XRD pattern for thermal decomposition product of $[Ni(N_2H_4)_3]Cl_2 \subset SiO_2$ under Ar atmosphere; (c) TEM and (d) XRD pattern of thermal decomposition product of $[Ni(N_2H_4)_3]Cl_2 \subset SiO_2$ under Ar/H_2 atmosphere.

Heterogeneous Nucleation and Seeded Growth of Ni⊂SiO$_2$

The next approach we explored to synthesize zero-valent nickel nanorods was to use Ni⊂SiO$_2$ as seeds to induce heterogeneous nucleation and subsequent growth. An extensively studied, mature method that possesses the necessary attributes is termed electroless nickel plating.[72] Electroless nickel plating is characterized by the selective

reduction of nickel ions at the surface of a catalytically active substrate (*e.g.* Ni, Fe, Co, Rh, Pd, Pt) that is submerged into an aqueous solution (bath) of nickel ions. Continued reduction and deposition on the substrate is accomplished through the catalytic activity of the deposit itself. This auto-catalytic process results in the deposition of nickel metal, nickel phosphide, or nickel boride depending on the reducing agent employed. The procedure is typically used in the coatings industry when wear resistance, hardness, and corrosion protection are required. Electroless nickel plating has also been used in the synthesis of nanoscale particle and rods for catalytic hydrogenations.[70,86,87]

There are four reducing agents commonly employed in electroless nickel plating baths: Sodium borohydride, sodium hypophosphite (NaH_2PO_2), hydrazine, and borane dimethylamine (($CH_3)_2NH \cdot BH_3$) (DMAB). All are structurally similar because they contain at least one reactive hydrogen. To suppress homogeneous nucleation (formation of new particles) in solution, organic acids or their salts are introduced to complex with and reduce the reactivity of nickel ions, rendering them kinetically inaccessible to the reducing agent in the solution. Extensive studies have determined optimum conditions (*e.g.* temperature, ligands, pH, etc.) for plating with each of the reducing agents.[72] Electroless nickel plating with $NaBH_4$ requires elevated temperatures (>70°C) and highly alkaline conditions (pH = 14), making it an unsuitable reducing agent for heterogeneous nucleation and growth of $Ni \subset SiO_2$.

Electroless nickel plating using N_2H_4 requires slightly alkaline conditions and undesirable temperatures (Table 2a), but has the added advantage of resulting in the deposition of only Ni^0 (Scheme 5). The commonly accepted net equation in Scheme 5 shows that N_2 is the by-product of N_2H_4 decomposition, thereby resulting in a pure Ni^0

deposit assuming the gases evolved are not trapped in interstices within the growing

lattice. The reaction was carried out according to the conditions shown in Table 2a and

the evolution of gases was visually observed throughout the duration of the reaction. The

XRD pattern (Figure 23a) of the product obtained after plating shows the presence of fcc-

Ni, although there is unaccounted amounts of amorphous material as evidenced by a

hump around 62 two-theta degrees. The average crystallite size calculated from XRD

using the Scherrer equation shows an increase from 9.1 nm to 10.9 nm, suggesting

growth occurred. TEM micrographs (Figure 23b and 23c) show an average increase of

silica encapsulated Ni^0 particle size from 13.6 ± 2.8 nm to 16.1 ± 4.6 nm (Figure 23d).

Table 2a. Nickel Bath Composition (N_2H_4)		Table 2b. Nickel Bath Composition (DMAB)	
$Ni \subset SiO_2$	1.40 mg/mL	$Ni \subset SiO_2$	1.65 mg/mL
$Ni(CH_3COO)_2 \bullet 4H_2O$	0.120 M	$Ni(CH_3COO)_2 \bullet 4H_2O$	0.030 M
$Na_2C_4H_4O_6 \bullet 2H_2O$	0.016 M	$C_6H_{12}O_7$	0.17 M
$C_6H_{12}O_7$	0.15 M	DMAB	0.060 M
$N_2H_4 \bullet H_2O$	0.40 M	pH (NH_4OH)	6.8
pH (NaOH)	9.6	Temperature	20 °C
Temperature	75 °C	Time	2.0 h
Time	0.5 h		

Scheme 5.

$$[NiL_m]^{-(n-2)} \rightleftharpoons [Ni^{2+} + mL^{-n}] + N_2H_4 + H_2O \xrightarrow{Ni^0} Ni^0 + 2H^+ + mL^{-n} + N_2 + H_2$$
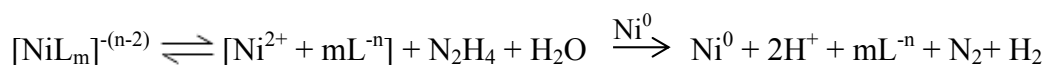
where $L = CH_3COO^-$, $C_4H_4O_6^{2-}$, and/or $C_6H_{12}O_7$; $m = 0$-6 Although there is discernible

growth present inside the capsules, (Figure 23d) there are also Ni^0 particles that are not

contained within the silica nanocapsules as shown in the upper left corner of Figure 23b

and scattered throughout Figure 23c. This could be the result of either or both homogeneous nucleation and the complete etching of silica capsules to yield free Ni^0 particles. The TEM micrographs provide evidence for both pathways. The upper left corner of Figure 23b shows anisotropic Ni^0 particles suggesting that growth started in the interior of the nanocapsule, but after some time the nanocapsule was etched away by the high temperature alkaline environment. Furthermore, the background of the anisotropic particles shows a different contrast to that of the TEM grid, possibly attributed to the remnants of etched silica capsules. Further evidence of etching is shown by the thin silica nanocapsule present in the center of Figure 23c and the ruptured nanocapsule in the upper left hand corner. However, this does not account for the spherical free Ni^0 particles observed in both micrographs. These particles could be the result of homogeneous nucleation events and/or the complete etching of a silica nanocapsule. Clearly, the temperature and pH conditions used in the synthesis are too harsh to maintain silica nanocapsule integrity and suppress homogeneous nucleation events from occurring making hydrazine an unsuitable reducing agent for the seeded growth of nickel nanorods.

The conditions previously cited for electroless nickel plating using DMAB as the reducing agent are inert towards silica nanocapsule degradation (Table 2b). Reduction of nickel salts with DMAB results in Ni^0/Ni_xB_y amorphous materials (Scheme 6), but the mechanism of Ni_xB_y formation remains unknown.[72] XRD (Figure 24) was used to probe the evolution of this material as a function of each reaction step. Electroless nickel plating using DMAB as the reducing agent in the presence of $Ni \subset SiO_2$ resulted in amorphous material (Figure 24). After calcination of amorphous material$\subset SiO_2$ under H_2, the XRD pattern shows fcc-Ni. Comparing the starting material to the final product, it

is clear that the crystallite size has drastically increased as evidenced by the decrease in peak width from the starting material.
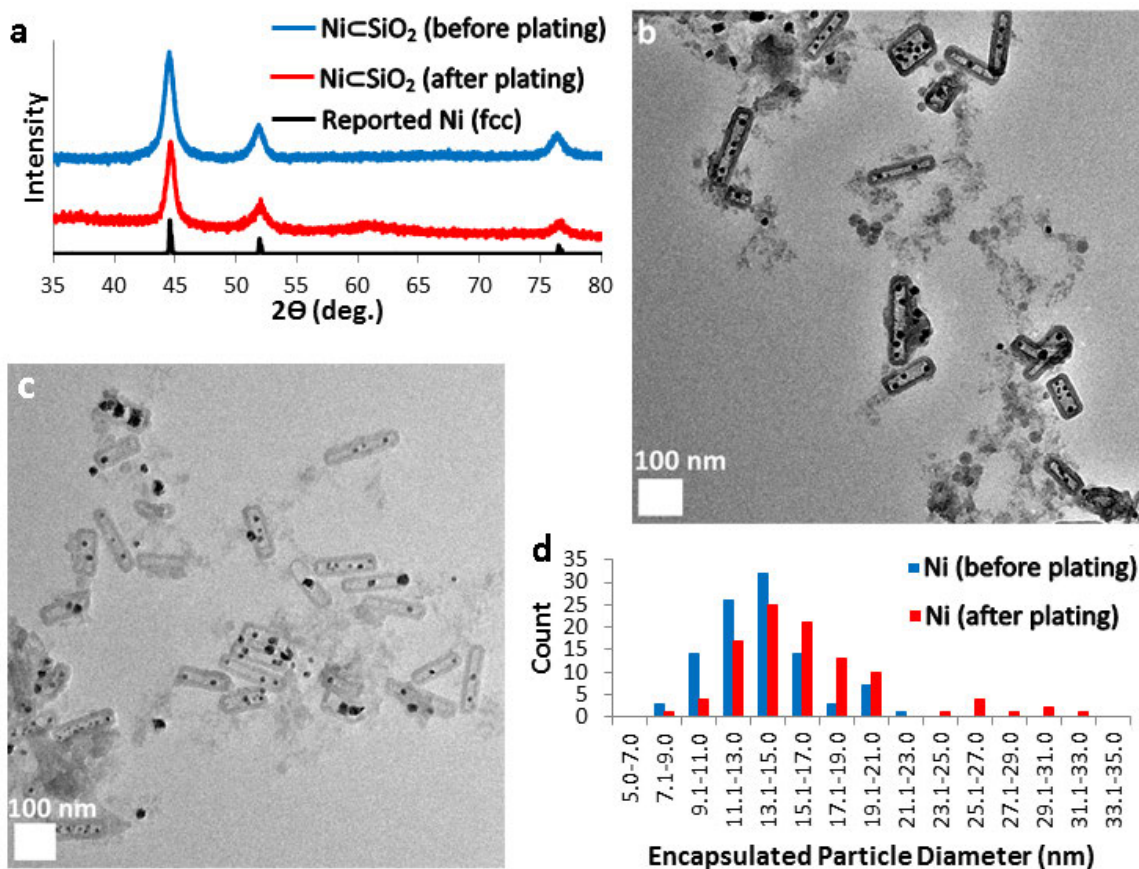
Figure 23. (a) XRD pattern of Ni⊂SiO$_2$ before and after plating; (b) and (c) TEM micrographs of Ni⊂SiO$_2$ after plating; (d) Particle size distribution histogram of encapsulated Ni particles.

Scheme 6.

$$3[NiL_m]^{-(n-2)} \rightleftharpoons 3[Ni^{2+} + mL^{-n}] + 2(CH_3)_2NHBH_3 + 6H_2O \xrightarrow{Ni^0} 3Ni^0 + 2(CH_3)_2NH_2^+$$

$$+ 2B(OH)_3 + 4H^+ + 3mL^{-n} + 3H_2$$
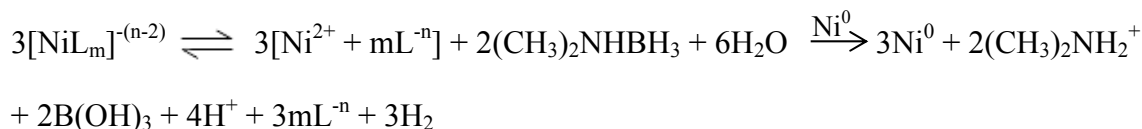
where L = CH$_3$COO$^-$, C$_6$H$_{12}$O$_7$; m = 0-6
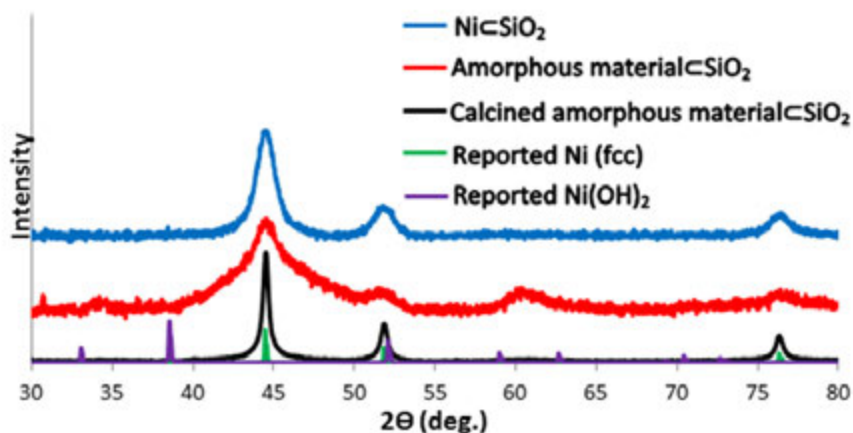
Figure 24. Evolution of XRD patterns during EN plating using DMAB as reducing agent.

The XRD pattern (Figure 24) shows crystal growth occurred during the reaction, but it does not confirm whether it was the result of heterogeneous or homogeneous nucleation. The Ni^{2+} concentration of the growth solution shown in Table 2b (*i.e.* no $Ni \subset SiO_2$) was monitored by UV/Vis spectroscopy (Figure 25a) to test for solution stability. The spectra show that the absorbance maximum at 390 nm does not decrease as a function of time for two hours suggesting that Ni^{2+} is not consumed. However, the absorbance maximum at 664 nm does show a slight decrease in absorbance (0.004) after two hours corresponding to decrease of 4.3 μmol (2.8% of the total Ni^{2+} concentration) and may possibly be due to self-nucleation events. Another control experiment was run to determine whether the presence of silica nanocapsules (*i.e.* no encapsulated Ni^0) could act as a substrate and allow for discernible homogeneous nucleation events by monitoring Ni^{2+} concentration. Silica nanocapsules obtained from etching $[Ni(N_2H_4)_3]Cl_2 \subset SiO_2$ with HCl (Figure 10a) were submerged into the growth solution shown in Table 2b and the absorption spectra were recorded at different times (Figure 25b). The increase in

absorption at 390 nm between the spectra can be attributed to incomplete removal of colloidal silica nanocapsules that scatter light and give an errant increase in absorption. Due to silica colloids present in solution, not much can be concluded as to whether self-nucleation events were occurring or not. The aforementioned silica nanocapsules were subjected to thermal treatment under H_2 to reduce any nickel species present on the surface of silica nanocapsules. The diffractogram (Figure 25c) shows there is no apparent difference between silica nanocapsules and the thermally treated silica nanocapsules. The three control experiments strongly suggest the growth solution is kinetically stable and without a catalyst heterogeneous or homogeneous nucleation events do not occur or occur to a degree which is scarcely detected by UV/Vis spectroscopy and XRD analysis.
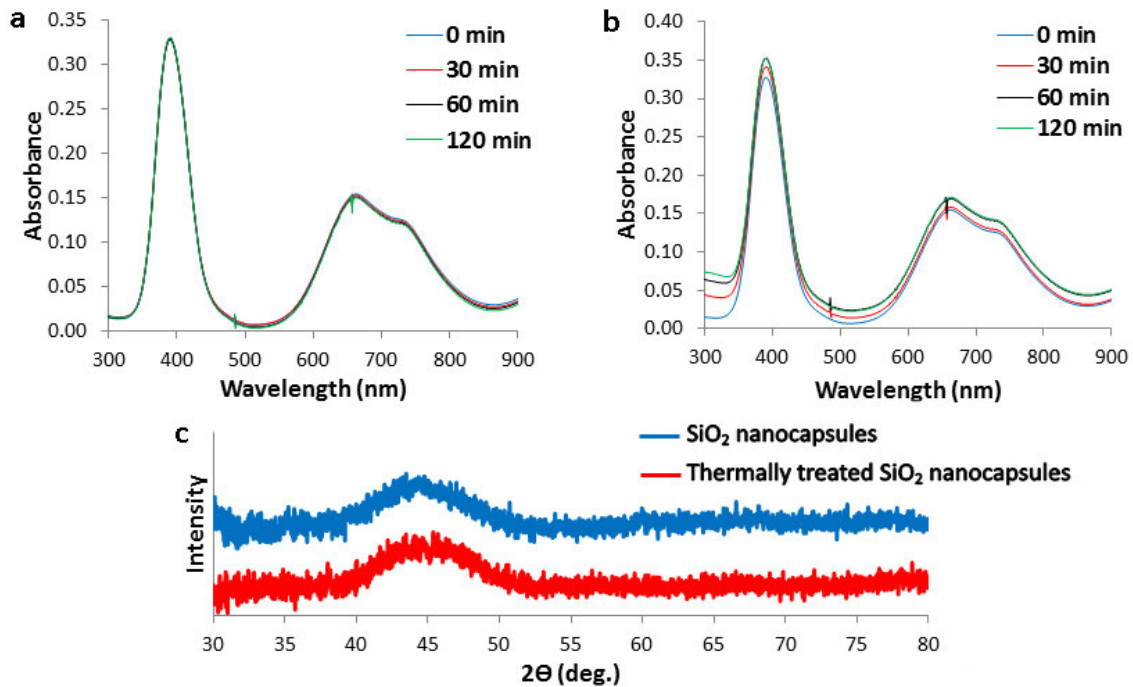

Figure 25. (a) UV/Vis spectra of growth solution shown in Table 2b; (b) UV/Vis spectra of growth solution shown in Table 2b in the presence of silica nanocapsules (*i.e.* no Ni^0 particles); (c) XRD data of silica nanocapsules (blue) and silica nanocapsules placed into growth solution, dried, and then thermally treated under H_2 (red).

Particle size distribution histograms (Figure 26d) were obtained from TEM micrographs (Figure 26b and 26c) of Ni⊂SiO$_2$ after electroless nickel plating using DMAB as the reducing agent and show no growth within the nanocapsule (8.6 ± 1.9 nm and 8.6 ± 1.3 nm before and after, respectively). Agglomerated material was observed outside the nanocapsule (Figure 26c) suggesting homogeneous nucleation may have occurred. Another possible explanation for the observed agglomeration could be due to catalytic reduction of nickel ions on Ni^0 particles that were not encapsulated by silica (Figure 26a). There is also a considerable amount of small Ni^0 particles on the edge of a silica nanocapsule shown in Figure 26b which could be the result of nucleation events occurring on the surface of silica capsules.

Treating Ni⊂SiO$_2$ with a nickel growth solution containing DMAB resulted in formation of new material, but the material was not contained within the silica nanocapsule. However, when Ni⊂SiO$_2$ was treated with a nickel growth solution containing N$_2$H$_4$ as the reducing agent internal growth of Ni^0 particles was observed. One important difference between the two experiments is the medium in which the reactions take place. Conditions used for electroless nickel plating using N$_2$H$_4$ etch silica, while the conditions used for electroless nickel plating using DMAB are inert towards silica. The TEM micrograph obtained from electroless nickel plating using N$_2$H$_4$ as a reducing agent (Figure 23c) shows a ruptured nanocapsule in the upper left corner. The ruptured nanocapsule likely resulted in an increase of mass transfer and led to a considerable amount of Ni^0 filling the interior. A similar observation is made in the center of Figure 23c. The silica nanocapsule is very thin and the particle contained within the nanocapsule is considerably larger than the particles contained in thicker silica capsules. These

observations lead to the conclusion that there is a mass transfer hindrance of bulky nickel complexes into the nanocapsule interior during electroless nickel plating using DMAB, resulting in the absence of particle growth within the silica nanocapsule.
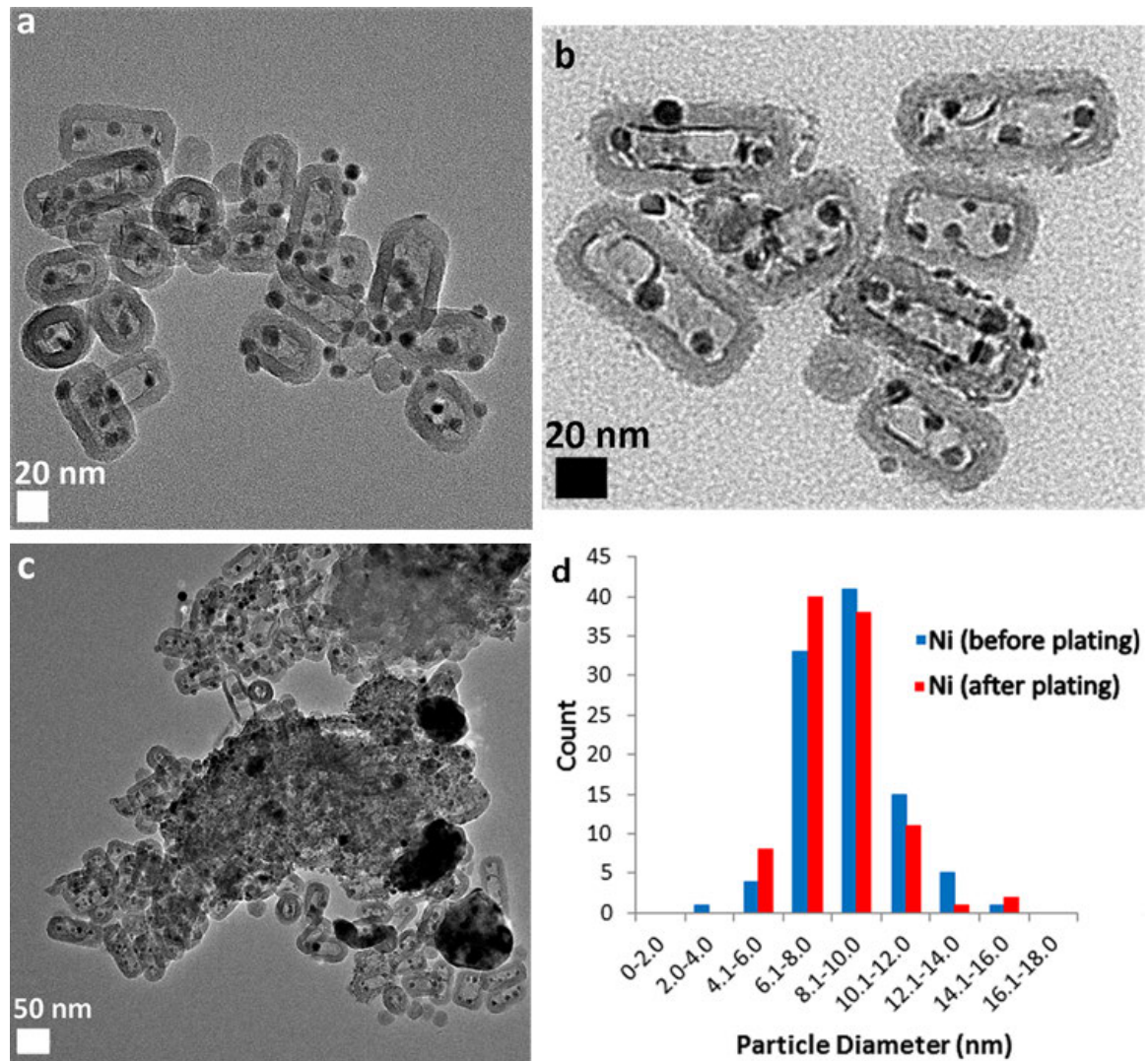
Figure 26. (a) TEM micrograph of Ni⊂SiO$_2$ before plating; (b) and (c) TEM micrograph of Ni⊂SiO$_2$ after plating; (d) Particle size distribution histogram for Ni⊂SiO$_2$ before and after plating using DMAB as reducing agent.

Typically, colloidal silica particles are microporous if formed in alkaline solution and especially if formed at elevated temperature[88], making it difficult to effectively diffuse molecules to internal metal nanoparticles for catalytic reactions. In addition, calcination of silica increases the condensation and crosslinking of the silica matrix, thereby increasing density and decreasing porosity.[89,90] The latter is demonstrated by comparing the TO mode of Si-O-Si asymmetric bond stretching vibration of as-SiO$_2$ to c-SiO$_2$ using FTIR spectroscopy (Figure 27a). The position of the Si-O-Si band is correlated with the density of silica; it blue-shifts as silica becomes more dense.[91] There is clearly a shift of the Si-O-Si stretch to higher wavenumbers upon calcination, suggesting a more dense silica material.

UV/Vis transmission spectroscopy also provides evidence that calcination of silica nanocapsules results in increased density. As-synthesized and calcined silica nanocapsules were dispersed in ethanol to form 0.22 mg mL^{-1} dispersions and their visible light transmittance was monitored (Figure 27b). From the spectra you can clearly see that c-silica nanocapsules transmit less light than as-silica nanocapsules. The difference in transmittance can be attributed to differences in density between the silica nanocapsules. As transmittance decreases, the intensity of scattered and/or absorbed light increases

(1) $$T = \frac{I}{I_0}, \text{ where } I = I_0 - I_{abs} - I_{sca}$$

where T is transmittance, I is the intensity of radiation reaching the detector, I_0 is the intensity of incident radiation, I_{abs} is the intensity of light absorbed by the silica nanocapsules, and I_{sca} is the intensity of light scattered by the silica nanocapsules.[92] Silica

is optically transparent rendering the intensity of absorbed light negligible and thus the differences in transmitted light can be solely attributed to I_{sca}. The light scattering intensity at perpendicular incidence to the diameter of a dielectric cylinder is proportional to the refractive index of the dispersion

$$(2) \qquad\qquad I_{sca} \propto (m^2 - 1)^2$$

where m is the refractive index of the dispersion.[92] The refractive index of colloidal solutions can be described by the refractive indices of the dispersed and continuous phases

$$(3) \qquad\qquad m = \phi_d n_d + \phi_c n_c$$

where ϕ_d, n_d and ϕ_c, n_c are the volume fractions and refractive indices for the dispersed and continuous phases, respectively.[93] Based on the equations, the transmittance of silica nanocapsule dispersions will decrease when the refractive index of the dispersed increases. Because the refractive index for silica increases as the density of silica increases,[90] the decrease in transmittance for c-SiO$_2$ can be attributed to an increase in the silica nanocapsule density. However, there are also other factors that contribute to scattering that cannot be overlooked such as particle aggregation and dispersion homogeneity.

Furthermore, it has been shown that increased porosity from as-synthesized silica colloids is necessary to allow sufficient mass transfer into and out of silica shell materials for reactions to occur at the core.[94,95,96] There are several methods in the literature to increase silica porosity94[97,98,99,100] that will be actively explored and possibly allow for increased mass transfer to the catalytic nickel center and permit seeded growth to occur preferentially within the silica nanocapsule.
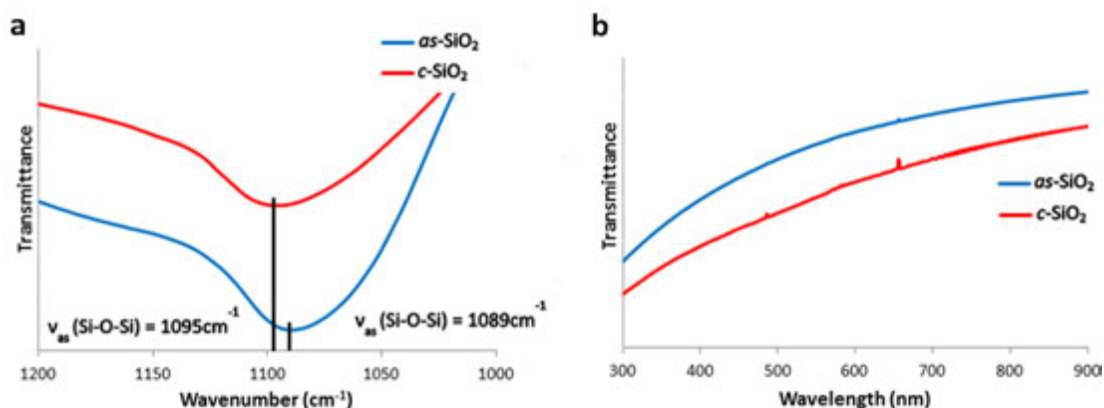
Figure 27. (a) FTIR spectrum of *as*-SiO$_2$ and *c*-SiO$_2$; (b) UV/Vis transmittance spectrum of *as*-SiO$_2$ and *c*-SiO$_2$.

Conclusion

In summary, a method for the reproducible and potentially scalable synthesis of silica templated Ni^0 particles displaying strong magnetic behavior was developed. Unlike most reported methods for the synthesis of silica encapsulated metal particles, our approach encapsulates numerous particles in one shell. We have shown that Ni⊂SiO$_2$ can be synthesized by chemical reduction of [Ni(N$_2$H$_4$)$_3$]Cl$_2$⊂SiO$_2$ using NaBH$_4$ followed by calcination under H$_2$. Preliminary data suggest that varying the amount of NiCl$_2$ while keeping the same surfactant/water ratio allows size control of the Ni^0 particles. Transformation of ill-defined Ni-B⊂SiO$_2$ to well-defined crystalline fcc-Ni has been proposed to occur through atomic migration of newly formed Ni^0 particles. Silica encapsulated Ni^0 particles hold promise for the synthesis of nickel nanorods for use in bimetallic heterostructured hydrogen storage materials.

Attempts to synthesize Ni^0 nanorods encapsulated by silica included thermal decomposition of [Ni(N$_2$H$_4$)$_3$]Cl$_2$⊂SiO$_2$ and seeded growth of Ni⊂SiO$_2$. Thermal

decomposition resulted in formation of a mobile species and significant amounts of nanocapsules were found void of Ni^0 particles. Seeded growth was carried out *via* electroless nickel plating using N_2H_4 and DMAB as reducing agents. Discernible growth was observed inside the nanocapsule using N_2H_4, but the silica shell was etched during growth due to the high temperature and alkaline conditions employed. Experiments conducted under low temperature and pH neutral conditions using DMAB resulted in no internal growth of encapsulated Ni^0 particles. We believe the main cause for this is minimal shell porosity of calcined silica which hinders sufficient mass transfer of bulky nickel complexes. Future work will focus on carrying out the growth reaction using DMAB with $Ni \subset SiO_2$ particles that have increased shell porosity. If successful, the metal nanorods will be used as building blocks for bimetallic heterostructured hydrogen storage materials.

Experimental

Materials

Polyoxyethylene (20) cetyl ether, tetraethyl orthosilicate (≥99.0%), borane dimethylamine complex (97%), and gluconic acid (50 wt. % in H_2O) were purchased from Sigma-Aldrich. Hydrazine monohydrate (100%, hydrazine 64%) and sodium borohydride (≥98%) were purchased from Acros. Cyclohexane (99.9%), diethylamine (reagent), sodium hydroxide (99.4%), and ammonium hydroxide (28.54%) were purchased from Fisher. Nickel (II) chloride hexahydrate (≥99.9% Ni) was purchased from Strem. Hydrogen gas (99.995%) and argon gas (99.996%) were purchased from

Linweld. Nickel (II) acetate tetrahydrate (reagent) was purchased from J.T. Baker.

Sodium tartrate dihydrate (97%) was purchased from Mallinckrodt.

Calcination Experiments

Calcination experiments were conducted in a three-zone Lindberg/Blue M Tube

Furnace (Thermo Scientific) equipped with a 3" diameter quartz tube. Specifications: 240

V, 3.8 kW, 50/60 Hz, 16 A. A heating rate of 10°C min^{-1} was used in all experiments.

Synthesis of $[Ni(N_2H_4)_3]Cl_2 \subset SiO_2$

In a typical synthesis, Brij 58 (8.5 g, 7.6 mmol) was weighed into a 100 mL three-

neck round-bottom flask. The flask was equipped with a Teflon stir bar and stainless steel

thermocouple. The contents were sealed using a septa and a glass adapter and brought

onto a Schlenk line. The flask was purged with argon and then cyclohexane (15 mL) was

added. The contents dissolved upon heating to 50°C in an oil bath and this temperature

was maintained throughout the experiment. Under stirring, NiCl$_2$•6H$_2$O aqueous solution

(1.5 mL, 1.2 mmol) was added to the colorless transparent solution and stirred until a

green, transparent homogeneous reverse microemulsion was obtained. Then, N$_2$H$_4$•H$_2$O

(0.45 mL, 9.3 mmol N$_2$H$_4$•H$_2$O) was added dropwise, causing a gradual color change to

pink. After stirring for 3 h, diethylamine (1.1 mL) was added, followed by TEOS (3.44

mL, 15.4 mmol) addition. This was allowed to stir for 2 h. The product was isolated by

centrifugation (5000 rpm for 5 min) and washed several times with isopropanol. The

product was dried in air at 60°C overnight. Yield: 1.2 g.

Synthesis of Ni-B⊂SiO$_2$

    [Ni(N$_2$H$_4$)$_3$]Cl$_2$⊂SiO$_2$ (1.2 g, ≈ 1.2 mmol Ni^{2+}) was placed into a 125 mL Erlenmeyer flask equipped with a Teflon stir bar. To this, H$_2$O (30 mL) was added and the suspension sonicated for 15 min. The flask was placed onto a stir plate at room temperature and under stirring, freshly prepared NaBH$_4$ aqueous solution (5 mL, 2.4 mmol) was added dropwise, but fast, causing evolution of gases and a color change to black. The suspension was allowed to stir for 30 min before being collected by centrifugation and washed with water and ethanol. The product was dried under vacuum at for 6 h.

Calcination of Ni-B⊂SiO$_2$ Under Ar/H$_2$

    Ni-B⊂SiO$_2$ (0.6 g) was placed into a ceramic combustion boat. The boat was placed into the center of a tube furnace equipped with 3" diameter quartz tube. The quartz tube was fitted with an inlet adapter used to funnel H$_2$/Ar into the system and the outlet adapter was equipped with an oil bubbler. A gas mixer equipped with Dwyer flow controls was used to purge the tube with a mixture of Ar (50 mL min^{-1}) and H$_2$ (10 mL min^{-1}) gases for 30 min and the flow rates were maintained throughout the duration of the experiment. The temperature was then ramped from room temperature to 500°C at 10°C min^{-1} and was sustained at this temperature for 2 h before convection cooling to room temperature. The diffraction pattern showed face-centered cubic nickel crystal structure.

Electroless Nickel Plating Using N$_2$H$_4$•H$_2$O

    In a 50 mL Erlenmeyer flask, Ni(CH$_3$COO)$_2$•4H$_2$O (0.5843 g, 3.000 mmol) was dissolved in H$_2$O (25 mL). Then in order, Na$_2$C$_4$H$_4$O$_6$•2H$_2$O (0.0924 g, 0.402 mmol),

$C_6H_{12}O_7$ (1.4760 g solution, 3.7622 mmol $C_6H_{12}O_7$), and $N_2H_4 \cdot H_2O$ (0.49 mL, 10. mmol) were added to the flask. The pH was adjusted to 9.6 with NaOH using a Fisher Scientific Accumet AB 15/ 15+ bench-top pH meter. The contents were transferred to an Erlenmeyer flask containing $Ni \subset SiO_2$ (0.0351 g). The suspension was heated in air to 75°C ($\approx$ 20 min) on a Fisher Scientific Isotemp Basic Hotplate monitored with a mercury thermometer. The reaction was allowed to proceed for 30 min at 75°C and the evolution of gas was observed throughout the duration of the experiment. The product was collected by centrifugation, washed several times with H_2O, and then dried in air at 60°C.

Electroless Nickel Plating Using DMAB

In a 50 mL Erlenmeyer flask, $Ni(CH_3COO)_2 \cdot 4H_2O$ (0.1500g, 0.6027 mmol) was dissolved in H_2O (20 mL). Then in order, $C_6H_{12}O_7$ (1.3215 g solution, 3.3684 mmol $C_6H_{12}O_7$) and DMAB (0.0708g, 1.20 mmol) were added to the flask. The pH was adjusted to 6.8 with NH_4OH. The contents were transferred to an Erlenmeyer flask containing $Ni \subset SiO_2$ (0.0330 g). The suspension was heated to 45°C ($\approx$10 min). The reaction was allowed to proceed for 2.5 h at 45°C and the evolution of gas was observed throughout the duration of the experiment. The product was collected by centrifugation, washed several times with H_2O, and then dried in air at 60°C.

Structural Characterization

X-ray Diffraction

Powder XRD data were measured using Co $K\alpha_1$, $K\alpha_2$ split radiation (45 kV, 40 mA, λ_{avg} = 1.7903 Å) on a PANalytical X'Pert PRO diffractometer equipped with a theta-theta vertical mode goniometer, incident Fe filter, an air cooled X'Celerator Real Time

Multiple Strip (RTMS) detector, and spinner stage. The spectra were converted to Cu Kα radiation for comparison to standard patterns. Powder XRD data were also measured using Cu Kα_1, Kα_2 split radiation (45 kV, 40 mA, λ_{avg} = 1.5418 Å) on a PANalytical X'Pert PRO diffractometer equipped with a theta-theta vertical mode goniometer, diffracted beam Ni filter, an air cooled X'Celerator RTMS detector, and spinner stage. Quantitative determinations of phase abundances were determined using Rietveld analysis on X'Pert HighScore Plus and GSAS software (reported as weight percent). The XRD samples were prepared by placing powders onto a background-less polycarbonate sample holder.

Transmission Electron Microscopy

TEM was conducted using a FEI Technai G2 F20 field emission TEM and a scanning transmission electron microscope (STEM) operating at 200 kV (point-to-point resolution < 0.25 nm and a line-to-line resolution of < 0.10 nm). TEM samples were prepared by placing 2-3 drops of dilute ethanol suspensions onto carbon-coated copper grids. The composition of Ni⊂SiO_2 structures were characterized by energy dispersive spectroscopy (EDS) line scans in STEM mode.

Size and Morphology Analysis

Particle dimensions were measured with ImageJ. In all cases, measurements and statistics were obtained for >50-100 [Ni(N_2H_4)$_3$]Cl_2 complexes, silica nanocapsules, or Ni^0 particles. Averages are reported ± standard deviations.

Scanning Electron Microscopy

SEM was conducted using a FEI Quanta 250 FE-SEM (maximum resolution of 1.2 nm) equipped with secondary and backscattered electron detectors and IXRF Systems

EDS system. SEM samples were prepared by placing 2-3 drops of dilute ethanol suspensions onto glass cover slips.

Optical Characterization

Fourier Transform Infrared Spectroscopy

Vibrational infrared spectra were recorded with a Bruker IFS66 V FT-IR spectrometer (transmittance mode) equipped with a DTGS detector with 16 scans at a resolution of 4 cm^{-1}. The samples were prepared by dilution with KBr and pressed into a pellet. Background spectra were collected under identical conditions. Samples were continuously purged with dry N_2 to minimize water vapor absorbance.

Ultraviolet-Visible Spectroscopy (UV/Vis)

Absorption spectra were measured with a StellarNet-Black-Comet diffuse reflectance spectrometer equipped with a 2048 pixel Charge Coupled Device (CCD) detector, slit size of 100 μm, and a spectral range of 280-900 nm. Dark and light background spectra were obtained for all samples. The sample was placed at the same distance from the probe as the dark and light spectra background standards. Absorption spectra were also measured with a photodiode-array Agilent 8453 UV/Vis spectrophotometer. Solvent absorption was recorded and subtracted from all spectra.

REFERENCES

[1] Balat, M. *Int. J. Hydrogen Energy* **2008,** 33, 4013-4029.

[2] Marbán, G.; Valdés-Solís, T. *Int. J. Hydrogen Energy* **2007,** 32, 1625-1637.

[3] U.S. Department of Energy, Energy Efficiency and Renewable Energy. http://www1.eere.energy.gov/hydrogenandfuelcells/storage/current_technology.html (accessed September 2012).

[4] Bogdanović, B.; Schwickardi, M. *J. Alloys Compd.* **1997,** 253,1-9.

[5] Liang, G.; Huot, J.; Boily, S.; Van Neste, A.; Schulz, R. *J. Alloys Compd.* **1999,** 292, 247-252.

[6] Orimo, S.; Fujii, H. *Appl. Phys. A* **2001,** 72, 167-186.

[7] Ershova, O.G.; Dobrovolsky, V.D.; Solonin, Yu.M.; Khyzhun, O. Yu..; Koval, A. Yu. *J.Alloys Compd.* **2008,** 464, 212-218.

[8] Milanese, C.; Girella, A.; Bruni, G.; Berbenni, V.; Cofrancesco, P.; Marini, A.; Villa, M.; Matteazzi, P. *J. Alloys and Cmpd.* **2008,** 465, 396-405.

[9] Züttel, A. *Naturwissenschaften* **2004,** 91, 157-172.

[10] Leung, W.B.; March, N.H.; Motz, H. *Phys. Lett. A* **1976,** 56, 425-426.

[11] Rock, P.A. *Chemical Thermodynamics*; MacMillan: New York, 1969; p 478.

[12] Zhou, L. *Renewable Sustainable Energy Rev* **2005,** 9, 395-408.

[13] Beebe, B.A.; Biscoe, J.; Smith, W.R.; Wendell, C.B. *J. Am. Chem. Soc.* **1947,** 69, 95-101.

[14] Zhou, Y.P.; Zhou, L. *Sep. Sci. Technol.* **1998,** 33, 1787-1801.

[15] Ding, F.; Yakobson, B.I. *Front. Phys.* **2011,** 6, 142-150.

[16] Farha, O.K.; Eryazici, I.; Jeong, N.C.; Hauser, B.G.; Wilmer, C.E.; Sarjeant, A.A.; Snurr, R.Q.; SonBinh, N.T.; Yazaydin, O.A.; Hupp, J.T.; *J. Am. Chem. Soc.* **2012,** 134, 15016-15021.

[17] Bogdanović, B.; Sandrock, G. *MRS Bull.* **2002,** 9, 712-716.

[18] Taylor, H. *Annu. Rev. Phys. Chem.* **1961,** 12, 127-150.

[19] Robell, A.J.; Ballou, E.V.; Boudart, M. *J. Phys. Chem.* **1964,** 68, 2748-2753.

[20] L'Homme, G.A.; Boudart, M.; D'Or, L. *Bull. Acad. Roy. Belg. Cl. Sci.* **1966,** 52, 1206-1248, 1249-1270.

[21] Benson, J.E.; Kohn, H.W.; Boudart, M. *J. Catal.* **1966,** 5, 307-313.

[22] Nowak, E.J.; Koros, R.M. *J. Catal.* **1967,** 7,50-56.

[23] Sancier, K.M.; Inami, S.H. *J. Catal.* **1968,** 11, 135-142.

[24] Sinfelt, J.H.; Lucchesi, P.J. *J. Am. Chem. Soc.* **1963,** 85, 3365-3367.

[25] Fujimoto, K. Catalyst Design Based on Spillover Theory. In *New Aspects of Spillover Effect in Catalysis for Development of Highly Active Catalysts*, Inui, T., Fujimoto, K.., Uchijima, T., Masai, M., Eds.; Studies in Surface Science and Catalysis 77; Elsevier Science: New York, 1993; Vol. 77, pp 9-16.

[26] Crucq, A.; Degols, L.; Lienard, G.; Frennet, A. In *Studies in Surface Science and Catalysis 17*; Germain, J., Pajonk, G., Teichner, S. J., Eds.; Elsevier: Amsterdam, 1983; p 137.

[27] Cheng, H.; Chen, L.; Cooper, A.C.; Sha, X.; Pez, G.P. *Energy Environ. Sci.* **2008,** 1, 338-354.

[28] Conner, W.C.; Falconer, J.L. *Chem. Rev.* **1995,** 95, 759-788.

[29] Bloch, J.; Mintz, M.H. *J. Alloys Compd.* **1997,** 253, 529-541.

[30] Tan, Z.; Chun, C.; Heilweil, E.; Bendersky, L.A. *Int. J. Hydrogen Energy* **2011,** 26, 9702-9713.

[31] Oguchi, H.; Tan, Z.; Heilweil, E.J.; Bendersky, L.A. *Int. J. Hydrogen Energy* **2010,** 35,1296-1299.

[32] Tan, Z.; Heilweil, E.J.; Bendersky, L.A.; In-situ Kinetics Studies on Hydrogenation of Transition Metal(=Ti, Fe) Doped Mg Films. *Mater. Res. Soc. Symp. Proc.* **2010,** 1216-W04-04.

[33] Zaluska, L.; Zaluska, A.; Tessier, P.; Strom-Olsen, J.O.; Schulz, R.; *J. Alloys Compd.* **1995,** 217, 295-300.

[34] Bobet, J.L.; Grigorovab, E.; Khrussanovab, M.; Khristovb, M.; Radevb, D.; Peshevb,

P. *J. Alloys Compd.* **2002,** 345, 280-285.

[35] Tzanétakis, P.; Hillairet, J.; Revel, G. *Phys. Status Solidi B* **1976,** 75, 433-439.

[36] Zhang, J.; Fisher, T.S.; Ramachandran, P.V.; Gore, J.P.; Mudawar, I. *J. Heat Transfer* **2005,** 127, 1391-1399.

[37] Bérubé, V.; Radtke, G.; Dresselhaus, M.; Chen, G. *Int. J. Energy Res.* **2007,** 31, 637-663.

[38] Gao, C.; Lu, Z.; Yin, Y. *Langmuir* **2011,** 27, 12201-12208.

[39] Over, H.; Hertel, T.; Bludau, H. *Phys. Rev. .* **1993,** 48, 5572-5578.

[40] Fan, F.; Liu, D.; Wu, Y.; Duan, S.; Xie, Z.; Jiang, Z.; Tian, Z. *J. Am. Chem. Soc.* **2008,** 130, 6949–6951.

[41] Xia, Y.; Yang, P.; Sun, Y.; Wu, Y.; Mayers, B.; Gates, B.; Yin, Y.; Kim, F.; Yan, H. *Adv. Mater.* **2003,** 15, 353-389.

[42] Sugawara, A.; Coyle, T.; Hembree, G. G.; Scheinfein, M. R. *Appl. Phys. Lett.* **1997,** 70, 1043-1045.

[43] Jorritsma, J.; Gijs, M. A. M.; Kerkhof, J. M.; Stienen, J. G. H. *Nanotechnology* **1996,** 7, 263-265.

[44] Yang, C.; Sheu, H.; Chao, K. *Adv. Funct. Mater.* **2002,** 12, 143-148.

[45] Yu, Y.; Chang, S.; Lee, C.; Wang, C. *J. Phys. Chem. B* **1997,** 101, 6661-6664.

[46] Braun, E.; Eichen, Y.; Sivan, U.; Ben-Yoseph, G. *Nature* **1998,** 391, 775-778.

[47] Jorgenson, M.R.; Bartl, M.H. *J. Mater. Chem.* **2011,** 21, 10583-10591.

[48] Obare, S. O.; Jana, N. R.; Murphy, C. J. *Nano Lett.* **2001,** 1, 601-603.

[49] Cao, G.; Liu, D. *Adv. Colloid Interface Sci.* **2008,** 136, 45-64.

[50] Ajayan, P.M.; Iijima, S. *Nature* **1993,** 361, 333-334.

[51] Kitaura, R.; Nakanishi, R.; Saito, T.; Yoshikawa, H.; Awaga, K.; Shinohara, H. *Angew. Chem. Int. Ed.* **2009,** 48, 8298-8302.

[52] Martín, J.; Maiz, J.; Sacristan, J.; Mijangos, C. *Polymer* **2012,** 53, 1149-1166.

[53] Napolsky, K.S.; Eliseev, A.A.; Knotko, A.V.; Lukahsin, A.V.; Vertegel, A.A.; Tretyakov, Y.D. *Mater. Sci. Eng., C* **2003,** 23, 151-154.

[54] Crowley, T.A.; Ziegler, K.J.; Lyons, D.M.; Erts, D.; Olin, H.; Morris, M.A.; Holmes, J.D. *Chem. Mater.* **2003,** 15, 3518-3522.

[55] Zhang, Z.; Dai, S.; Blom, D.A.; Shen, J. *Chem. Mater.* **2002,** 14, 965-968.

[56] Huang, M.H.; Choudrey, A.; Yang, P. *Chem. Commun.* **2000,** 1063-1064.

[57] Lee, K.; Lee, S.; Cheon, J. *Adv. Mater.* **2001,** 13, 517-520.

[58] Han, Y.; Kim, M.; Stucky, G.D. *Chem. Mater.* **2000,** 12, 2068-2069.

[59] Yang, X.; Tang, H.; Cao, K.; Song, H.; Sheng, W.; Wu, Q. *J. Mater. Chem.* **2011,** 21, 6122-6135.

[60] Woo Park, J.; Chae, E. H.; Kim, S.H.; Ho Lee, J.; Kim, J.W.; Mi Yoon, S.; Choi, J. *Mater. Chem. Phys.* **2006,** 97, 371-378.

[61] Nicholls, D.; Swindells, R. *J. Inorg. Nucl. Chem.* **1968,** 30, 2211-2217.

[62] Bruynooghe, S.; Bertin, F.; Chabli, A.; Gay, J.-C.; Blanchard, B.; Couchaud, M. *Thin Solid Films* **1998,** 313-314, 722-726.

[63] Sacconi, L.; Sabantini, A. *J. Inorg. Nuclear Chem.* **1963,** 25, 1389-1393.

[64] Nicholls, D.; Rowley, M.; Swindells, R. *J. Chem. Soc. (A)* **1966,** 950-952.

[65] Cordente, N.; Respaud, M.; Senocq, F.; Casanove, M.; Amiens, C.; Chaudret, B. *Nano Lett.* **2001,** 1, 565-568.

[66] Yu, K.; Kim, D.J.; Chung, H.S.; Liang, H. *Mater. Lett.* **2003,** 57, 3992-3997.

[67] Ghosh, S.; Ghosh, M.; Rao, C.N.R. *J. Cluster Sci.* **2006,** 18, 97-111.

[68] Ni, X.; Su, X.; Yang, Z.; Zheng, H. *J. Cryst. Growth* **2003,** 252, 612-617.

[69] Wu, Z.; Ge, S.; Zhang, M.; Li, W.; Mu, S.; Tao, K. *J. Phys. Chem. C* **2007,** 111, 8587-8593.

[70] Deng, J.; Li, H.; Wang, W. *Catal. Today* **1999,** 51, 113-125.

[71] Lee, S.; Chen, Y. *Ind. Eng. Chem. Res.* **1999,** 38, 2548-2556.

[72] Glenn O. Mallory; Juan B. Hajdu; Juan B. Hajdu. Chapter 1: The Fundamental Aspects of Electroless Nickel Plating. In *Electroless Plating: Fundamentals and Applications*, American Electroplaters and Surface Finishers Society, 1990, p. 14.

[73] Li, H.; Li. H.; Deng, J. *Mater. Lett.* **2001,** 50, 41-46.

[74] Mueller, R.; Kammler, H.K.; Wegner, K.; Pratsinis, S.E. *Langmuir* **2003,** 19, 160-165.

[75] Legrand, J.; Taleb, A.; Gota, S.; Guittet, M.-J.; Petit, C. *Langmuir* **2002,** 18, 4131-4137.

[76] Lu, K.; Zhu, X. *Thin Solid Films* **2009,** 517, 4479-4483.

[77] Berger, S.V. *Acta Chem. Scand.* **1953,** 7, 611-622.

[78] Bartholomew, C.H. Sintering and Redispersion of supported Metals: Perspectives from the Literature of the Past Decade. In *Catalyst Deactivation 1997*; Bartholomew, C.H., Fuentes, G.A., Eds.; Studies in Surface Science and Catalysis; Elsevier Science: Amsterdam, The Netherlands, 1997; Vol. 111, pp 585-592.

[79] Nakayama, T.; Arai, M.; Nishiyama, Y. *J. Catal.* **1984,** 87, 108-115.

[80] Arai, M.; Ishikawa, T.; Nishiyama, Y. *J. Phys. Chem.* **1982,** 86, 577-581.

[81] Boudjahem, A.G.; Monteverdi, S.; Mercy, M.; Bettahar, M.M. *J. Catal.* **2004,** 221, 325-334.

[82] Dahlberg, K.A.; Schwank, J.W. *Chem. Mater.* **2012,** 24, 2635-2644.

[83] Patil, K.C. *Proc. Indian Acad. Sci. (Chem. Sci.)* **1986,** 96, 459-464.

[84] Chen, X.; Zhang, T.; Zheng, M.; Wu, Z.; Wu, W.; Li, C. *J. Catal.* **2004,** 224, 473-478.

[85] Lif, J.; Skoglundh, M.; Löwendahl, L. *Appl. Catal., A* **2002,** 228, 145-154.

[86] Li, H.; Xu, Y. *Mater. Lett.* **2001,** 51, 101-107.

[87] Li, H.; Lin, H.; Xie, S.; Dai, W.; Qiao, M.; Lu, Y.; Li, H. *Chem. Mater.* **2008,** 20, 3936-3943.

[88] Ller, R.K. Colloidal Silica-Concentrated Sols. *The Chemistry of Silica: Solubility Polymerization, Colloid and Surface Properties, and Biochemistry,* Wiley & Sons: New York, 1979; p 328.

[89] Minhao, Y.; Henderson, M.J.; Gibaud, A. *Thin Solid Films* **2009,** 517, 3028-3035.

[90] Ller, R.K. Silica Gels and Powders. *The Chemistry of Silica: Solubility Polymerization, Colloid and Surface Properties, and Biochemistry,* Wiley & Sons: New York, 1979.

[91] Nam, C.W.; Woo, S.I. *Thin Solid Films* **1994,** 237, 314-319.

[92] Kerker, M. Analysis of Particle Size. *The Scattering of Light and Other Electromagnetic Radiation*; Academic Press: New York, 1969.

[93] Heller, W. *Phys. Rev.* **1945,** 68, 5-10.

[94] Hu, Y.; Zhang, Q.; Goebl, J.; Zhang, T.; Yin, Y. *Phys. Chem. Chem. Phys.* **2010,** 12, 11836-11842.

[95] Gao, C.; Zhang, Q.; Lu, Z.; Yin, Y. *J. Am. Chem. Soc.* **2011,** 133, 19706-19709.

[96] Lee, J.; Park, JC.; Bang, JU.; Song, H. *Chem. Mater.* **2008,** 20, 5839-5844.

[97] Zhao, L.; Zhao, Y.; Han, Y. *Langmuir* **2010,** 26, 11784-11789.

[98] Park, JC.; Lee, HJ.; Jung, HS.; Kim, M.; Kim, HJ.; Park, H.; Song, H. *ChemCatChem* **2011,** 3, 755-760.

[99] Zhang, Q.; Zhang, T.; Ge, J.; Yin, Y. *Nano Lett.* **2008,** 8, 2867-2871.

[100] Zhang, T.; Ge, J.; Hu, Y.; Zhang, Q.; Aloni, S.; Yin, Y. *Angew. Chem. Int. Ed.* **2008,** 47, 5806-5811.